

Cite this: *Chem. Sci.*, 2024, 15, 6363

All publication charges for this article have been paid for by the Royal Society of Chemistry

# Ultrafast symmetry-breaking charge separation in Perylenemonoimide-embedded multichromophores: impact of regioisomerism†

Rupam Roy,<sup>‡a</sup> Sakshi Chawla,<sup>‡b</sup> Vikas Sharma,<sup>‡a</sup> Arun K. Pal,<sup>id c</sup> Yogita Silori,<sup>bd</sup> Ayan Datta,<sup>id \*c</sup> Arijit K. De<sup>id \*b</sup> and Apurba Lal Koner<sup>id \*a</sup>

Symmetry-breaking charge separation (SB-CS) has recently evolved as an emerging concept offering its potential to the latest generation of organic photovoltaics. However there are several concerns that need to be addressed to reach the state-of-the-art in SB-CS chemistry, for instance, the desirable molecular geometry, interchromophoric distance and extent of electronic coupling. To shed light on those features, it is reported herein, that *ortho*-functionalized perylene monoimide (PMI) constituted regioisomeric dimer and trimer derivatives with varied molecular twisting and electronic conjugation have been synthesized. In steady-state photophysical studies, all the dimers and trimer derivatives exhibit a larger bathochromic shift in the emission spectra and a significant reduction of fluorescence quantum yield in polar DMF. Among the series of multichromophores, *ortho*- and self-coupled dimers display the strikingly different optical feature of SB-CS with a very fast charge separation rate ( $\tau_{CS} = 80.2$  ps) upon photoexcitation in DMF, which is unveiled by femtosecond transient absorption (fs-TA) studies. The SB-CS for two dimers is well-supported by the formation of  $PMI^{*+}$  and  $PMI^{*-}$  bands in the fs-TA spectra. Further analysis of fs-TA data revealed that, among the other multichromophores the trimer also exhibits a clear charge separation, whereas SB-CS signatures are less prominent, but can not be completely disregarded, for the *meta*- and *para*-dimers. Additionally, the charge separation dynamics of those above-mentioned PMI derivatives are devoid of a kinetically favorable excimer or triplet formation. The evidence of a profound charge transfer phenomenon in the *ortho*-dimer is characterized by density functional theory (DFT) calculations on excited state electronic structures. The excitonic communications in the excited state electronic arrangements unravel the key role of dihedral twisting in SB-CS. The thermodynamic feasibility of CS ( $\Delta G_{CS}$ ) and activation barrier ( $\Delta G^\ddagger$ ) of the derivatives in DMF are established from the Rehm–Weller equation and Marcus's theory, respectively. This work is an in-depth study of the effect of mutual orientation of PMIs and regioisomerism in determining sustainable guidelines for using SB-CS.

Received 9th October 2023  
Accepted 20th March 2024

DOI: 10.1039/d3sc05325c

rsc.li/chemical-science

## Introduction

The phenomenon of symmetry-breaking charge separation (SB-CS) is a fundamental and sister concept for photoinduced

charge separation which has endowed a significant contribution to organic photovoltaics, organic photonics, and artificial photosynthesis.<sup>1</sup> The formation of multiple excitons (electron hole pairs) at the donor–acceptor interfaces of the optoelectronic devices *via* photoinduced SB-CS substantially improves the charge carrier mobility of excitons, thus reflecting on their greater performances in photovoltaic devices.<sup>2,3</sup> The SB-CS is more advantageous than charge separation in conventional donor (D)–acceptor (A) systems due to the occurrence of a minimum energy loss (<100 mV for SB-CS and ~500 mV for a D–A chromophore).<sup>4</sup> The SB-CS can be viewed as an electron transfer-mediated transformation of the symmetrical lowest excited states into an unsymmetrical stable charge-separated state (electrons and holes are spatially separated) in the presence of the surrounding environments.<sup>1,4,5</sup> Several factors such as mutual orientation of chromophores, distances between monomers created using variable spacer units, extent of electronic coupling, and more importantly, the surrounding

<sup>a</sup>Bionanotechnology Lab, Department of Chemistry, Indian Institute of Science Education and Research Bhopal, Bhopal Bypass Road, Bhauri, Bhopal, Madhya Pradesh 462066, India. E-mail: akoner@iiserb.ac.in

<sup>b</sup>Condensed Phase Dynamics Group, Department of Chemical Sciences, Indian Institute of Science Education and Research Mohali, Knowledge City, Sector 81, SAS Nagar, Punjab 140 306, India. E-mail: akde@iisermohali.ac.in

<sup>c</sup>School of Chemical Sciences, Indian Association for the Cultivation of Science, 2A and 2B Raja S. C. Mullick Road, Jadavpur, Kolkata, West Bengal 700032, India. E-mail: spad@iacs.res.in

<sup>d</sup>Department of Physics, University of Michigan, Ann Arbor, Michigan 48109, USA

† Electronic supplementary information (ESI) available: Synthesis procedure, theoretical calculations, steady-state spectroscopy, transient absorption study, electrochemical study. See DOI: <https://doi.org/10.1039/d3sc05325c>

‡ These authors contributed equally to this work.

dielectric medium markedly influence the rate of SB-CS.<sup>6–10</sup> Depending upon the occurrence of SB-CS, it can be categorized into two classes: intermolecular (a photosynthetic system in purple bacteria)<sup>11</sup> and an intramolecular SB-CS. Multichromophoric systems constituted of two or more identical chromophores are generally recognized as ideal scaffolds for the manifestation of intramolecular SB-CS.<sup>3,12,13</sup> By mimicking the highly efficient natural SB-CS system of the purple bacteria, judicious design strategies for chromophores featuring the desired photophysical properties have emerged as the first and foremost principle to create multichromophores for intramolecular SB-CS.<sup>14–16</sup> Uptonow, the most investigated intramolecular bichromophoric systems exploited for SB-CS include a variety of organic dyes such as 9,9-bianthryls,<sup>17,18</sup> BODIPY,<sup>19,20</sup> perylene,<sup>21,22</sup> perylene diimide (PDI),<sup>16,23</sup> terrylenediimide (TDI),<sup>24</sup> zinc dipyrin,<sup>25,26</sup> metalloporphyrin,<sup>27</sup> phthalocyanine<sup>28,29</sup> and so on.<sup>30–35</sup> Extensive studies showed that weakly electronically-coupled multichromophoric systems strongly favor SB-CS by exhibiting a rapid charge separation (timescale: 100 fs–10 ps) in polar solvents.<sup>3,36</sup>

In the gallery of organic  $\pi$ -conjugated materials for SB-CS, perylene imide (PI) embedded molecular dyads/triads have captured increased attention from physical-organic chemists due to the intriguing photophysical properties of PI's and the desired synthetic modifications on the perylene imide core.<sup>37–40</sup> Besides the previously mentioned features, the extreme electronic conjugation along their large  $\pi$ -skeletons and high electron affinity has bestowed on them an additional attribute

for better charge separation.<sup>41–43</sup> By exploiting those advantages, Wasielewski, Würthner and Kim, Xia, Hariharan and other groups have developed perylene diimide (PDI)-based multichromophoric systems exhibiting efficient charge separation and accomplishing long-lived charge-separated state *via* symmetry breaking.<sup>36,44–46</sup> A myriad of the literature reveals that the PDI chromophore has been extensively employed for SB-CS,<sup>47–49</sup> but such a phenomenon on its monoimide analog (perylene monoimide, PMI) has barely been researched. A few examples of PMI-based SB-CS have been reported, for instance, Hariharan and co-workers revealed SB-CS by direct *peri-peri* linked PMI dimer.<sup>50,51</sup> The *peri*-positions of the PMIs create a significant change in  $\pi$ -conjugation when compared to that of the PDIs, which can unfold distinct excited-state photophysical properties.<sup>52–56</sup> In this flourishing area, molecular engineering approaches have become a subject of great demand to attain a high CS rate. Also, the impact of regioisomerism on SB-CS remain elusive in the past literature. Therefore, in the quest to achieve fast SB-CS and to find the role of regioisomerism, we have developed a series of novel PMI-based multichromophoric architectures comprised of *ortho*-functionalized PMI-acetylene units (*o*-PMI-ac) connected *via* a phenyl (Ph) bridge at different positions (*ortho*-, *meta*-, *para*-) as well as a self-coupled PMI dimer and a 1,3,5-Ph-substituted PMI trimer (Fig. 1) which are abbreviated as *o*-Ph(*o*-PMI-ac)<sub>2</sub>, *m*-Ph(*o*-PMI-ac)<sub>2</sub>, *p*-Ph(*o*-PMI-ac)<sub>2</sub>, (*o*-PMI-ac)<sub>2</sub> and 1,3,5-Ph(*o*-PMI-ac)<sub>2</sub>, respectively. We have thoroughly investigated the effect of structural configuration for those multichromophores on the SB-CS process using

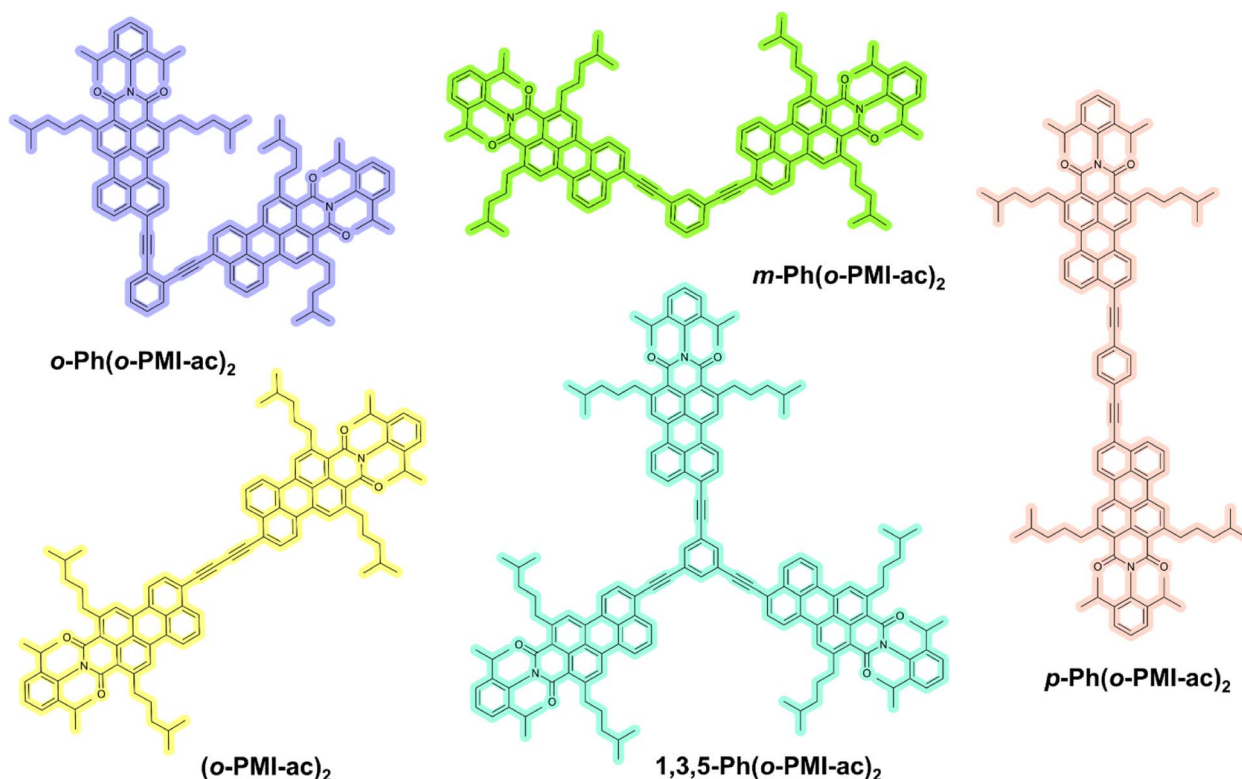


Fig. 1 Chemical structures of multichromophoric PMI derivatives investigated in this work.



steady-state absorption and emission, time-resolved fluorescence measurements, femtosecond transient absorption spectroscopy, and first-principles calculations. The study revealed that the *ortho*- and self-coupled PMI dimers show prominent SB-CS in a polar solvent, whereas it is prohibited in a weakly polar solvent. The structural distortion between the PMI monomers and the desired interchromophoric distance have led them to be suitable candidates for SB-CS with a weak-electronic coupling feature. Furthermore, the excited state CS phenomenon of the aforementioned derivatives is well-supported by in-depth theoretical calculations in addition to electrochemical investigation.

## Results and discussion

### Synthesis of PMI-coupled derivatives

The PMI-based multichromophores were synthesized by following the Sonogashira–Hagihara cross-coupling reaction giving a moderate to high yield (see Schemes S1 and S2,† and the detailed synthetic procedures for all compounds are provided in the ESI†). Briefly, *o*-PMI-ac was synthesized by a Ru-catalyzed regioselective *ortho*-functionalization of PMI, followed by selective monobromination at the *peri*-position, introduction of a TIPS-acetylene moiety in the presence of the  $\text{Pd}_2(\text{dba})_3\text{-P}(\text{o-tolyl})_3$  catalytic system and finally, deprotection of the TIPS. Next, the *o*-PMI-ac units were coupled at different positions of the phenyl core to obtain the desired multichromophores. All the intermediate and desired compounds were comprehensively characterized by  $^1\text{H-NMR}$  spectroscopy, and high-resolution mass spectrometry including ESI-MS and MALDI (Fig. S1–S18†). The self-coupled dimer was obtained as a side product in

the cross-coupling reactions. Here, the idea behind the introduction of an alkyne linker between the PMI and phenyl moieties was to extend the conjugation between the PMI units, thus modulating the electronic coupling, which is a crucial factor for the charge separation. In addition to that, bulky branched alkyl chains were incorporated in both *ortho*-positions of the PMI core that aided the significant increase in their solubility by disrupting the intense  $\pi$ – $\pi$  interaction among the multichromophores, which acts as a pre-requisite solubility factor for carrying out the spectroscopic investigations.

### Steady-state and time-resolved optical properties

The steady-state optical properties for all the synthesized derivatives were measured in three weakly polar to highly polar solvents namely toluene (Tol), chloroform ( $\text{CHCl}_3$ ), and *N,N*-dimethylformamide (DMF) with dielectric constant values of 2.38, 4.81, and 38.25, respectively. The optical purity of all the synthesized derivatives was validated from the superimposition of the absorption and excitation spectra in  $\text{CHCl}_3$  (see Fig. S19–S23 in the ESI†). Fig. 2a shows that the *o*-PMI-ac monomer ( $c = 2.0 \mu\text{M}$ ) in toluene exhibited a well-resolved absorption spectrum consisting of vibronic features at 512 nm, 483 nm and 452 nm corresponding to 0–0, 0–1, and 0–2 transitions, respectively. The molar extinction coefficient of the *o*-PMI-ac at its  $\lambda_{\text{max}}^{\text{abs}} = 512 \text{ nm}$  was found to be  $\epsilon_{\text{max}} = 41\,160 \text{ M}^{-1} \text{ cm}^{-1}$ . The *ortho*-PMI dimer, *i.e.*, *o*-Ph(*o*-PMI-ac) $_2$  showed an unusual absorption profile possessing  $\lambda_{\text{max}}^{\text{abs}}$  at 490 nm in comparison to the parent PMI chromophore in toluene. Here, the 0–1 vibronic band emerged as the predominant band rather than the 0–0 band ( $A_{0-0}/A_{0-1} = 0.84$ ), as discussed in the next section. On the other hand, in the normalized absorption spectra, *m*-Ph(*o*-

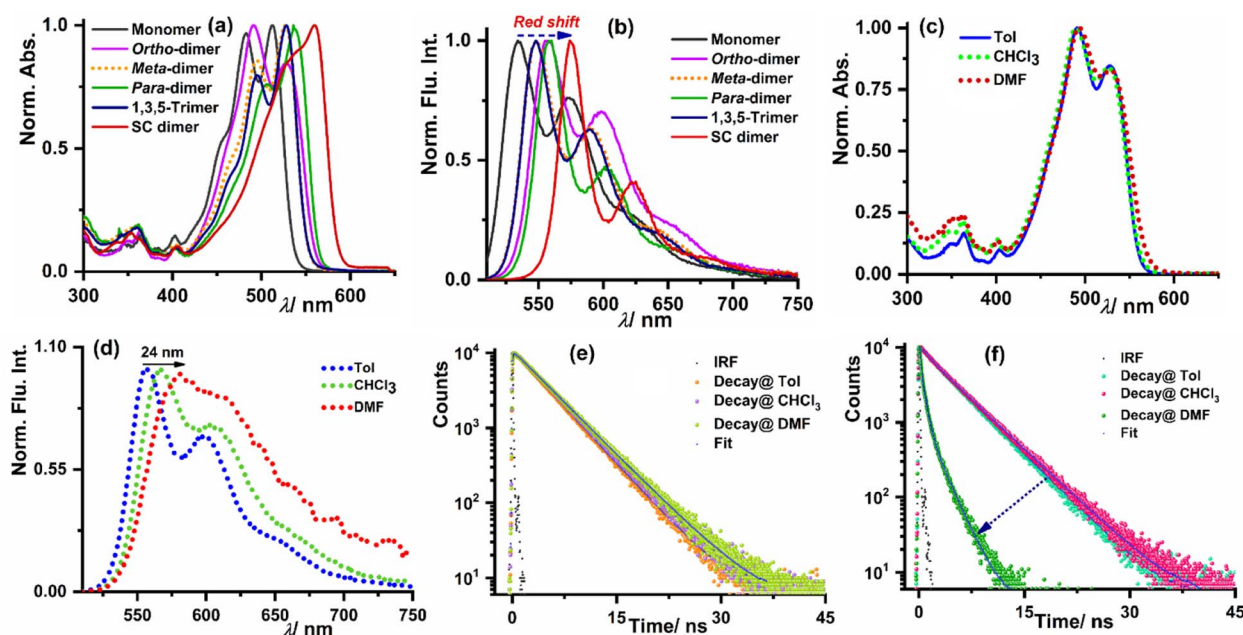


Fig. 2 Normalized (a) absorption and (b) emission spectra of all the investigated compounds including the reference monomer in toluene. (c) The normalized absorption and (d) normalized emission spectra of *o*-Ph(*o*-PMI-ac) $_2$  in three different solvents. The fluorescence lifetime decay of (e) *o*-PMI-ac monomer and (f) *o*-Ph(*o*-PMI-ac) $_2$  in three solvents.



PMI-ac)<sub>2</sub>, *p*-Ph(*o*-PMI-ac)<sub>2</sub>, 1,3,5-Ph(*o*-PMI-ac)<sub>3</sub> and self-coupled (*o*-PMI-ac)<sub>2</sub> dimer restored the nature of the vibronic progressions ( $A_{0-0}/A_{0-1} > 1.0$ ) at their characteristic bands in toluene which were akin to those in the reference monomer *o*-PMI-ac. The characterized vibronic features in the absorption spectrum for the self-coupled derivative were less sharp ( $\lambda_{\text{max}}^{\text{abs}} = 574 \text{ nm}$ ) in comparison to those of the other dimers and trimer derivatives. The evolution of strong vibronic progressions for all the PMI dimers/trimer derivatives is a sign of the coupling between the vinyl stretching mode ( $\sim 1250 \text{ cm}^{-1}$ ) of the perylene core and the  $S_0$ - $S_1$  electronic transition of the PMIs.<sup>14,57</sup> Notably, the dimers and trimer except *ortho*-PMI dimer showed a considerable bathochromic shift (17–48 nm) in their absorption spectra relative to the reference monomer because of the increased electronic conjugation between the two PMI monomer units through the phenyl linker. The UV-Vis. absorption spectra for all the derivatives delineated a negligible shift in their respective absorption maxima in weakly polar to highly polar solvents (Table 1), showing the insensitivity of their ground state electronic property towards the solvent polarity. The results of a concentration-dependent absorption study shown in Fig. S24 and S25† manifested no sign of aggregation of the multichromophores at the working concentration ( $c = 1.0 \text{ }\mu\text{M}$ ). To understand the excited-state optical properties, firstly, the fluorescence spectra of all the PMI derivatives in toluene were measured. On photoexcitation at 500 nm, the emission spectrum of the *o*-PMI-ac monomer in toluene displayed well-structured vibronic features mostly centered at 534 nm and 574 nm ( $\lambda_{\text{max}}^{\text{em}} = 534 \text{ nm}$ ) in conjunction with a weakly intense band at 624 nm. The emission profiles of the dimer and trimer derivatives in the same solvent (toluene) also revealed the appearance of a well-defined vibronic progression akin to *o*-PMI-ac, which was indicative of their existence in the monomer state, as shown in Fig. 2b. In stark contrast to the solvent polarity-independent absorption profiles, the emission spectra of the monomer and other derivatives exhibited a bathochromic

shift in highly polar DMF when compared to toluene (Fig. 2c and d for the *ortho*-PMI dimer, and Fig. S26–S30† for the other derivatives). It was noted that the emission spectra of the dimers and trimer became broad in DMF in comparison to toluene, which might be possible due to polar solvent-assisted charge separation *via* symmetry breaking. The SB-CS in a polar medium leads to the generation of charge-separated species which interact with the solvent's dipole, resulting in a red shift and a broadening of the spectra.<sup>50,58</sup> In addition, a marginal change in  $\lambda_{\text{max}}^{\text{abs}}$  and a relatively larger red shift in  $\lambda_{\text{max}}^{\text{em}}$  ensured to attain a large Stokes shift in DMF but not in the other two solvents (*e.g.*, for *ortho*-PMI dimer, the Stokes shifts were 66 nm, 77 nm, and 88 nm in toluene,  $\text{CHCl}_3$  and DMF, respectively). Subsequently, to gain further insights into the excited-state CS characteristics of such multichromophores, we measured the absolute fluorescence quantum yield ( $\Phi_{\text{F}}$ ) and the average fluorescence lifetime ( $\tau_{\text{avg}}$ ) in three solvents, as shown in Table 1. The  $\Phi_{\text{F}}$  values for the *o*-PMI-ac monomer in toluene and  $\text{CHCl}_3$  were 79% and 71%, respectively, but were decreased in DMF to give  $\Phi_{\text{F}}$  of 54% (note that the decrease of  $\Phi_{\text{F}}$  accounts for an inherent dipolar feature of PMI which is consistent with its asymmetric structure). Much to our delight, the dimer and trimer molecules expressed appreciably high  $\Phi_{\text{F}}$  values (QY range – 75–84%) in toluene, which drastically dropped in DMF ( $\Phi_{\text{F}} < 15\%$ ), for example, for the *ortho*-PMI dimer,  $\Phi_{\text{F}}$  (Tol) = 75%,  $\Phi_{\text{F}}$  ( $\text{CHCl}_3$ ) = 64% and  $\Phi_{\text{F}}$  (DMF) <1.0%. The reduction of  $\Phi_{\text{F}}$  values for multichromophores in polar DMF is ascribed to the activation of an additional non-radiative decay pathway in DMF. Similarly, the fluorescence lifetime measurement showed that the reference (*o*-PMI-ac) exhibited an increase in the fluorescence lifetime values with an increase in the solvent polarity (4.1 ns in Tol to 4.5 ns in DMF, Fig. 2e, Tables S1 and S2†) which is indicative of intramolecular charge transfer (ICT) characteristic present in *o*-PMI-ac. These ICT characteristics are further supported by an observed red shift in the steady state emission spectrum of the monomer (Fig. S26†) and the Lippert–Mataga plot in Fig. S31.† We estimate that a large change of dipole moment between the ground and excited electronic states ( $\Delta\mu = 4.77 \text{ Debye}$ ), is indicative of the presence of an ICT state. A similar behavior was observed for other PMI derivatives<sup>59</sup> and recently for terrylene monoimide.<sup>60</sup> The impact of the solvent polarity on the CT and locally excited (LE) states is widely recognized in the literature. As the solvent polarity increases, the CT energy level undergoes a gradual decrease because of the robust interaction between the solvent and solute. In contrast, the LE energy level remains relatively unaffected by the solvent polarity, and this is attributed to the small dipole moment associated with the LE state. This phenomenon implies that in high-polarity solvents, the CT state is energetically lower than the LE state while it is reversed in low-polarity solvents. A similar increase in the fluorescence lifetime with solvent polarity was observed for the PMI monomer,<sup>50</sup> aryl-substituted 9,9'-bianthryl derivatives<sup>61</sup> and substituted *N,N*-diphenyl-amine dyads.<sup>62</sup> The fluorescence decay of all the multichromophores in weakly and medium polar solvents were properly fitted with the mono-exponential function. In DMF, all these derivatives displayed bi-

Table 1 Photophysical properties of PMI derivatives in three solvents

Comp.	Solvent	$\lambda_{\text{max}}^{\text{abs}}$ <sup>a</sup> /nm	$\lambda_{\text{max}}^{\text{em}}$ <sup>b</sup> /nm	Stokes shift <sup>c</sup> /nm	$\Phi_{\text{F}}$ <sup>d</sup> /%
<i>ortho</i> -Dimer	Tol	491	557	66	75 ± 0.5
	$\text{CHCl}_3$	490	567	77	64 ± 0.5
	DMF	493	581	88	<1.0
<i>meta</i> -Dimer	Tol	527	548	21	74 ± 0.4
	$\text{CHCl}_3$	529	554	25	65 ± 0.4
	DMF	529	568	39	15 ± 1.7
<i>para</i> -Dimer	Tol	536	558	22	73 ± 0.7
	$\text{CHCl}_3$	540	566	26	64 ± 0.7
	DMF	540	574	34	12 ± 3.8
SC dimer	Tol	560	574	14	48 ± 1.4
	$\text{CHCl}_3$	560	580	20	64 ± 2.5
	DMF	558	588	30	<1.0

<sup>a</sup> Absorption maxima. <sup>b</sup> Emission maxima of four derivatives in the mentioned solvents. <sup>c</sup> Represents the Stokes shifts [ $\lambda_{\text{max}}^{\text{em}} - \lambda_{\text{max}}^{\text{abs}}$ ]. <sup>d</sup> The absolute QY was measured in three solvents using an integrating sphere. Quantum yield ( $\pm 5.0\%$ ).





exponential decay, indicating the evolution of a new excited-state species in polar DMF (Fig. 2f, S32, Tables S1 and S2†). A bi-exponential fluorescence decay may result from two potential reasons, the first involves a radiative charge recombination as observed in inorganic semiconductors. If this is the case, the spectra of the delayed emission would shift to a lower energy, reflecting the magnitude of the driving force for the SB-CS, as the emission would originate from the lower energy charge transfer (CT) state. The second possibility is that, due to the small driving force for SB-CS, the charges could recombine to the  $S_1$  state rather than directly to the ground state and would create a pseudo-equilibrium between the SB-CS state and the  $S_1$  state. This bi-exponential fluorescence lifetime was also observed for a spiro-conjugated perylenediimide dimer.<sup>36</sup> Based on the spectroscopic outcomes in DMF such as the bathochromic shift together with the broadening in the emission spectra, the profound reduction of absolute  $\Phi_{\text{Fl}}$  values and the prominent change in time-resolved decay, we anticipate the possibility of charge separation in polar DMF. The charge separation can facilitate the non-radiative decay channels competitive to the radiative pathway, from the  $S_1$  to CS state, and as a result, it diminishes the emission quantum efficiency of these multichromophoric PMI derivatives in DMF, that were not observed in toluene. Therefore, in the next section, we discuss the investigation of the excitonic interactions in the excited state together with their conformational studies by using computational methodologies.

## Electronic structure calculations

In this section, we discuss the molecular aggregation and excitonic communication in the excited state electronic structure. The discussion of the calculated absorption and emission spectrum have been provided in the ESI† together with the NTO plot in Fig. S33.† A brief description of Fig. 3a–c is provided in the ESI.† The long-range (Kasha-like) Coulomb exchange coupling ( $J_{\text{Coul}}$ ) values are calculated by using the transition charges from the electrostatic potential (TrESP) and the following equation:<sup>36,63</sup>

$$J_{\text{Coul}} = \frac{1}{4\pi\epsilon_0} \sum_i \sum_j \frac{q_i^{M_1} q_j^{M_2}}{|r_i^{M_1} - r_j^{M_2}|} \quad (1)$$

where  $q_i^M$  refers to the transition charges on the  $i$ th atom of monomer  $M$  and  $|r_i^{M_1} - r_j^{M_2}|$  which refers to the displacement vectors with respect to the centre of mass during an electronic transition. The calculated values for the three dimers are listed in Table 2. In the Kasha-like aggregation, the predominant nature of the coulombic coupling arises due to the large  $S_1 \leftarrow S_0$  transition electric dipole moment (TEDM).<sup>64</sup> The TEDM values of *ortho*-, *meta*- and *para*-PMI dimers are 5.61, 6.38 and 7.96 au, respectively, (see Table S3†). Therefore, the order of the  $J_{\text{Coul}}$  values should be  $J_{\text{Coul}}^{\text{para-}} > J_{\text{Coul}}^{\text{meta-}} > J_{\text{Coul}}^{\text{ortho-}}$ . However, the order is reversed in the present case:  $J_{\text{Coul}}^{\text{para-}} < J_{\text{Coul}}^{\text{meta-}} < J_{\text{Coul}}^{\text{ortho-}}$ . Therefore, the aggregation behavior based on the Kasha rule is unconventional here. This framework can be explained by considering the hole ( $t_h$ ) and the electron ( $t_e$ )

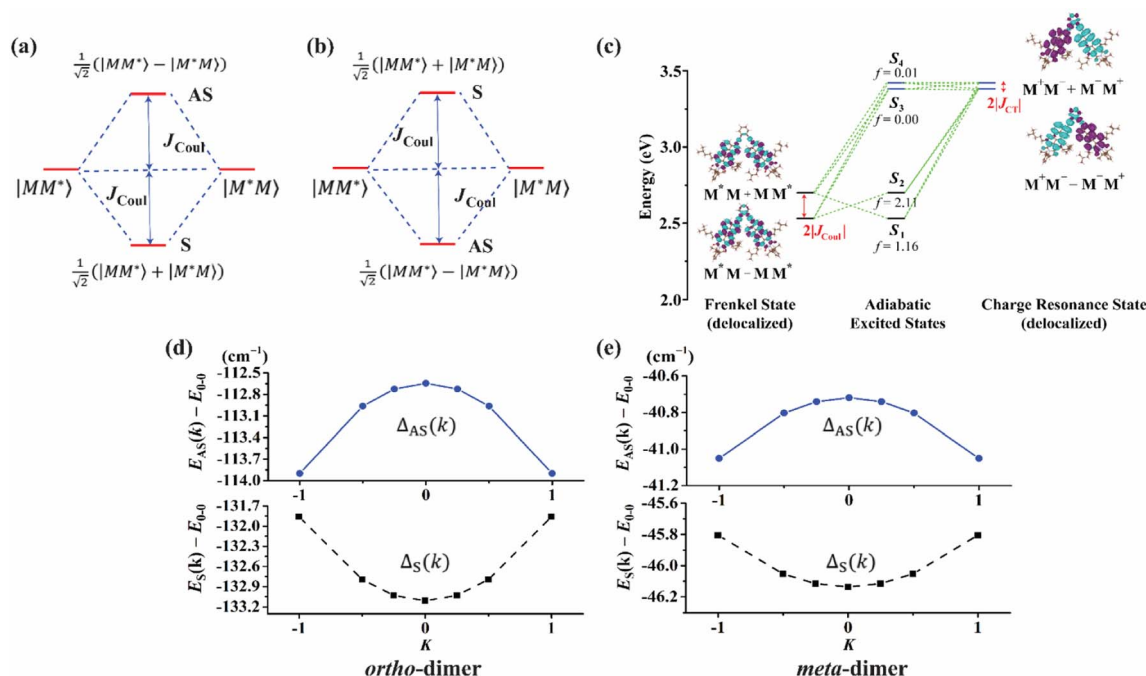


**Fig. 3** The framework of the conventional Kasha model (a) J-aggregate and (b) H-aggregate, where S = symmetric band and AS = antisymmetric band. In the excitonic coupling limit (a)  $t_h t_e > 0$  and (b)  $t_h t_e < 0$ . (c) The excited state energy diagram at the ground state optimized *ortho*-PMI dimer (PMI–PMI dihedral angle,  $\varphi = 44^\circ$ ) with a polarized continuum model of the chloroform solvent. The delocalized Frenkel and charge resonance excitons are the linear combination of the localized Frenkel ( $M^*M$  or  $MM^*$ ) and CT ( $M^-M^+$  or  $M^+M^-$ ) states of the monomers ( $M$ ). The coupling between the delocalized states results in adiabatic excited states ( $S_1$ – $S_4$ ). The oscillator strengths are denoted by  $f$ . (d) and (e) deviation from the Kasha-like aggregation in the *ortho*- and *meta*-dimer, respectively (eqn (2)–(4)).

**Table 2** The hole ( $t_h$ ) and electron ( $t_e$ ) transfer integral together with the short-range CT coupling ( $J_{CT}$ ), long-range Coulomb electrostatic coupling ( $J_{Coul}$ ) and energy shift of the antisymmetric band ( $\Delta_{AS}(k=0)$ ). Here,  $\varphi$  denotes the PMI–PMI dihedral angle in the dimer

(cm <sup>-1</sup> )	$t_h$	$t_e$	$J_{CT}$	$\Delta_{CT}$	$J_{Coul}$	$\Delta_{AS}(k=0)$
<i>ortho</i> -Dimer ( $\varphi = 20^\circ$ )	−2925	−165.7	−143.0	−2533	188.1	−543.5
<i>ortho</i> -Dimer ( $\varphi = 44^\circ$ )	−1296	−54.3	−20.5	−491.0	185.6	−112.6
<i>ortho</i> -Dimer ( $\varphi = 80^\circ$ )	−29.7	−13.8	0.12	−0.32	184.9	0.21
<i>meta</i> -Dimer	−802.6	−25.1	−4.55	−145.0	79.4	−46.1
<i>para</i> -Dimer	694.1	16.9	—	—	64.4	≥ 0

transfer integrals that allow the mixing of the Frenkel and CT excitons as previously demonstrated by Hestand *et al.* with oligoacenes<sup>65</sup> and later on by Zhong *et al.* with donor–acceptor chromophores.<sup>66</sup> In the excitonic coupling limit, the energy of the symmetric (S) and antisymmetric (AS) band is calculated by:

$$E_{S(AS)}(k) = E_{0-0} + \Delta_{S(AS)}(k) \quad (2)$$

where  $k$  is the wave vector and  $k=0$  refers to the bright state.  $E_{0-0}$  is the energy of the absorption maxima and  $\Delta_{S(AS)}(k)$  is the energy shift due to the excitonic coupling, expressed as:

$$\Delta_S(k) = \frac{E_{CT}}{2} - \sqrt{2(t_h^2 + t_e^2) + 4t_h t_e \cos\left(\frac{k}{2}\right) + \frac{E_{CT}^2}{4}} \quad (3)$$

$$\Delta_{AS}(k) = \frac{E_{CT}}{2} - \sqrt{2(t_h^2 + t_e^2) - 4t_h t_e \cos\left(\frac{k}{2}\right) + \frac{E_{CT}^2}{4}} \quad (4)$$

In the case of  $t_h = t_e$ ,  $\Delta_{AS}(k=0) = 0$ , indicates no energy shift. However, for  $t_h \neq t_e$ ,  $\Delta_{AS}(k=0) < 0$ , it clearly illustrates a red shift in the  $E_{AS}(k=0)$  value in eqn (2). Hence, it generates a H-like band which is completely unconventional with respect to the Kasha mechanism that relies on the Coulombic electrostatic interaction. The calculated  $t_h$ ,  $t_e$  and  $\Delta_{AS}(k=0)$  values are shown in Table 2. The  $t_h$  and  $t_e$  are not equal and are of same sign for all the cases. Therefore, for all the present cases ( $t_h t_e > 0$ ), the lower band is symmetric (S) and the upper band is antisymmetric (AS), as shown in Fig. 3a. For the *ortho*-PMI dimer, the  $\Delta_{AS}(k=0)$  is more negative (−112.6 cm<sup>-1</sup>) than that of the *meta*-PMI dimer (−46 cm<sup>-1</sup>) as shown by  $(E_{CT})_{ortho-} < (E_{CT})_{meta-}$  and  $(t_h t_e)_{ortho-} > (t_h t_e)_{meta-}$  in eqn (4). This results a more red-shifted (lower energy) value in  $E_{AS}(k=0)$  for the *ortho*-PMI dimer and shows H-aggregation, as illustrated in Fig. 3d and e, respectively. In the present scenario, the CT state is not detected among the first four singlet excited states of the *para*-PMI dimer but the state may arise in the higher energy states which is not considered here. Therefore, the  $E_{CT}$  of the *para*-PMI dimer is much larger than that of the others. Consequently, there is a blue-shift in the  $E_{AS}(k=0)$  value, which results in a J-like band. In a similar fashion, the interaction between the diabatic CS states can split them into two delocalized charge resonance states (DCR) with a splitting parameter of  $2|J_{CT}|$  (see Fig. 3c).<sup>67</sup> The CT couplings ( $J_{CT}$ ) are calculated with the  $t_e$  and  $t_h$  values and the energy differences between the virtual CT state ( $E_{CT}$ ) and the  $S_1$  state ( $E_{S_1}$ ).<sup>68</sup>

$$J_{CT} = -\frac{2t_e t_h}{E_{CT} - E_{S_1}} \quad (5)$$

The sign of  $t_e$  and  $t_h$  is dependent on the relative orientation of the nodal plane of HOMO and LUMO at an excitonic communication limit.<sup>68,69</sup> The  $J_{CT}$ s of *ortho*-PMI and *meta*-PMI dimers are calculated as −20.5 and −4.55 cm<sup>-1</sup> (Table 2). Hence, the possibility of the formation of the DCR state in the *meta*-PMI dimer is less because the CT coupling is not dominant when compared to the *ortho*-PMI dimer. The local electrostatic symmetry of the charge resonance state in the *ortho*-PMI dimer is broken by the solvent polarity and the hole/electron particularly occupies one monomeric unit which provides spontaneity to the generation of  $PMI^{+*}$ – $PMI^{*-}$ . The charges then recombine to produce a local exciton which is emitted to the ground state *via* a radiative or a non-radiative pathway.<sup>13,68</sup> In this process, the charge recombination can also occur directly from the initially created excited states which introduced a self-energy correction ( $\Delta_{CT}$ ) and this was determined by the expression:<sup>68</sup>

$$\Delta_{CT} = -\frac{2(t_e^2 + t_h^2)}{E_{CT} - E_{S_1}} \quad (6)$$

A self-energy correction of −491 cm<sup>-1</sup> in the *ortho*-PMI dimer indicates that there is a strong coupling between the local exciton and charge-separated excitons which also agrees with the non-Kasha aggregation behavior ( $\Delta_{AS}(k=0) < 0$ ) in the *ortho*-PMI dimer. However, a better justification of the Frenkel-CT mixing can be explained by considering the variations in intermolecular orientation,<sup>58</sup> see below.

The selected atoms in the dimer for a relaxed PES scan are shown in the Fig. S34.† As shown in Fig. 4a, the orbital overlap ( $J$ ) between the HOMO( $M_1$ ) and HOMO( $M_2$ ) or LUMO( $M_1$ ) and LUMO( $M_2$ ) is responsible for the SB-CS process whereas the  $J$  between the HOMO( $M_1$ ) and LUMO( $M_2$ ) is responsible for the charge recombination process to the ground state. Hence, it is relevant to investigate  $J_{HH}$ ,  $J_{LL}$  and  $J_{HL}$ . For the *ortho*-PMI dimer,  $J_{HH}$ ,  $J_{LL}$  and  $J_{HL}$  together with  $J_{H-1,H}$ ,  $J_{L,L+1}$ ,  $J_{H-1,L+1}$  and  $J_{H-1,L}$  are considered. The investigation is justified in Fig. S35,† where the HOMO − 1 of the neutral PMI reassembles with the singly occupied molecular orbital (SOMO) of the radical cation PMI while the LUMO of the neutral PMI molecule is identical with the SOMO of the radical anion PMI. Another reason is that the absorption maxima and CT states of the *ortho*-PMI dimer appeared mostly from the transitions between HOMO − 1,



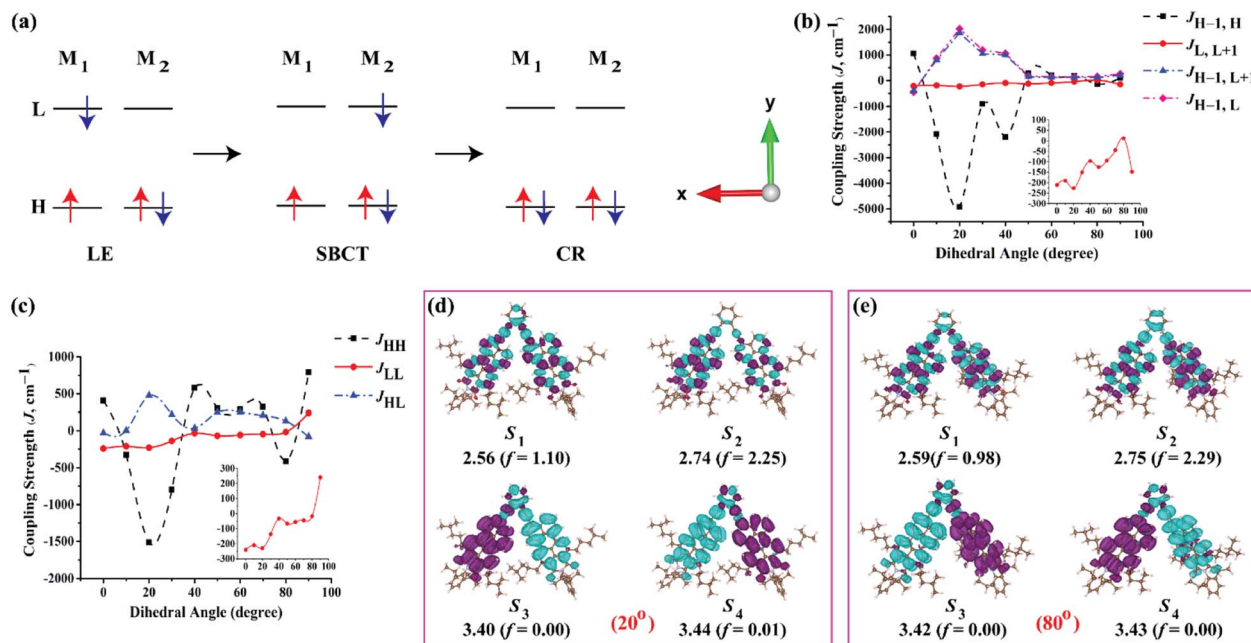


Fig. 4 (a) Scheme for the locally excited (LE), symmetry-breaking charge transfer (SB-CT) and charge recombination (CR) phenomenon in a dimer consisting of two monomeric units,  $M_1$  and  $M_2$  (H stands for HOMO and L stands for LUMO). (b) The variation of coupling strengths between HOMO – 1 and HOMO, LUMO and LUMO + 1, and HOMO – 1 and LUMO + 1 of monomer 1 and monomer 2, respectively, with dihedral angles between the two PMI units in the *ortho*-PMI dimer. (c) The variation of coupling strengths between the HOMOs, LUMOs and HOMO and LUMO of monomer 1 and monomer 2, respectively, with a dihedral angle between the two PMI units in *ortho*-PMI dimer. (d) and (e) The NTO plots with an isosurface of  $\pm 0.0002$  au corresponding to the first four singlet excited states in the *ortho*-PMI dimers with a dihedral angle between two PMI units of 20° (higher coupling strength) and 80° (lower coupling strength), respectively. The energies are in eV and calculated at the CAM-B3LYP/def2-SVP/PCM (chloroform) level of theory.

HOMO, LUMO and LUMO + 1 FMOs (Table S4 $^\dagger$ ). The variations of  $J$  with the PMI-PMI dihedral angle ( $\varphi$ ) are shown in Fig. 4b and c and Table S6 $^\dagger$ . For the *ortho*-PMI dimer, all types of coupling strengths are increasing with the decrease in the torsional angle. The geometry with  $\varphi \approx 20^\circ$  and  $40^\circ$  showed the maximum coupling strengths in  $J_{HH}$  and  $J_{H-1,H}$ . Comparatively lower values of the  $J_{LL}$  and  $J_{L,L+1}$  indicate that the electron transfer is suppressed, and the SB-CS occurs mainly *via* hole transfer between the monomeric units. The structure with  $\varphi \approx 80^\circ$  shows the minimal coupling in all cases. Therefore, the two structures  $\varphi \approx 20^\circ$  (maximum  $J$ ) and  $\varphi \approx 80^\circ$  (minimum  $J$ ) are considered for further studies. The NTO plots of the singlet excited states are shown in Fig. 4d and e, and the FMOs are shown in Fig. S36 $^\dagger$ . The characteristics of the Frenkel exciton in the  $S_1$  and  $S_2$  state, and the CR exciton in the  $S_3$  and  $S_4$  state are more prominent in  $\varphi \approx 20^\circ$  than in  $\varphi \approx 80^\circ$ . The absorption wavelength for the PMI monomer at CAM-B3LYP/def2-SVP/PCM (chloroform) level is 442 nm ( $f = 1.32$ ) whereas for  $\varphi \approx 20^\circ$  and  $\varphi \approx 80^\circ$ , the  $\lambda_{\text{abs}}^{\text{calc}}$  are 453 nm ( $f = 2.25$ ) and 451 nm ( $f = 2.29$ ), respectively, for the *ortho*-PMI dimer. The  $J_{\text{Coul}}$ ,  $J_{\text{CT}}$ ,  $\Delta_{\text{CT}}$  and  $\Delta_{\text{AS}}(k = 0)$  are listed in Table 2. The  $\varphi \approx 44^\circ$  corresponds to the full optimized structure. No significant changes have been observed in the  $J_{\text{Coul}}$  values in the  $\varphi \approx 20^\circ$ ,  $44^\circ$  and  $80^\circ$  structures. However,  $\varphi \approx 20^\circ$  carries a more negative  $J_{\text{CT}}$  ( $-143.0$  cm $^{-1}$ ) whereas  $\varphi \approx 80^\circ$  shows a minimal  $J_{\text{CT}}$  ( $0.12$  cm $^{-1}$ ). This shows that the structure with  $\varphi \approx 20^\circ$  it may be possible for it to show a larger excitonic occurrence ( $t_{\text{h}}t_{\text{e}} >$

$0$ ). $^{68}$  Consequently, a high negative  $\Delta_{\text{CT}}$  value corresponding to that structure refers to a significant Frenkel-CT mixing, which is an indication of the formation of an unconventional Kasha H-band. A large red-shift of the asymmetric band at  $k = 0$  confirms the deviation. The lower values of  $J_{H-1,L}$  with respect to the  $J_{H-1,H}$  shows that the rate of charge recombination is relatively small, unlike that of SB-CS. The *meta*- and *para*-PMI dimers are both rigid for the excited-state phenomenon and hence, do not show any significant variation in the orbital overlap with the interchromophoric orientations, as shown in Fig. S37 $^\dagger$ .

The energy of the first excited singlet states of the *ortho*-PMI dimer against the variation in the PMI-PMI dihedral angle is plotted in Fig. S38 $^\dagger$  which indicates the formation of an excimer-like structure. $^{70}$  The structure corresponding to the minima of this plot nearly agrees with the optimized  $S_1$  structure ( $\varphi = 38.5^\circ$ ), as shown in Fig. S39 $^\dagger$ . The solvent polarity simplifies the Frenkel-CT mixing in the excited state which introduces an amount of the CT characteristic to the  $S_1$  and breaks down the adiabaticity of the state in the *ortho*-PMI dimer, which is also evident from the larger Stokes shift and is comparable to the others (Tables 1 and S5 $^\dagger$ ). This results in a decrease in fluorescence lifetime, and hence, proceeds to an ultrafast SB-CS, as recently discussed by Hong *et al.* $^{14}$  and Qin *et al.* $^{71}$  with perylene bisimide dimer and perylene monoimide dimer, respectively. Furthermore, Marcus's theory is appropriate here to explain the electron transfer process as the SB-CS





process relies on the nonadiabatic electron transfer (NAET).<sup>72</sup> In this context, the NAET is predominantly dependent on Marcus's parameters: (i) driving force for the CS ( $\Delta G_{CS}$ ), (ii) reorganization energy ( $\lambda_{total}$ ), and (iii) electronic coupling ( $J_{HL}$ ). For the *ortho*-PMI dimer, the  $\Delta G_{CS}$  values in toluene, chloroform, and DMF are 0.46, 0.11 and  $-0.19$  eV, respectively, (calculated using the Rehm–Weller equation as discussed later). The internal  $\lambda$  ( $\lambda_i$ ) is calculated by using the optimized ionic structures at both their ground-state and excited-state. The contribution of solvent in  $\lambda$  ( $\lambda_s$ ) is also calculated in different solvents as discussed in the ESI.† Here,  $\lambda_{total} = \lambda_i + \lambda_s$ . A schematic showing an explanation of the Marcus parameters in SB-CS is captured in Fig. S40† and the calculated values are provided in Table S7.† The lower value of  $\Delta G_{CS}$  and the higher value of  $\lambda_{total}$  with the increase of solvent polarity clearly signifies that in DMF, the SB-CS occurs spontaneously. This finding is confirmed by calculating the activation barrier for the NAET:

$$\Delta G^\ddagger = (\Delta G_{CS} + \lambda_{total})^2 / 4\lambda_{total} \quad (7)$$

The  $\Delta G^\ddagger$  values are found to decrease with increase of the polarity of the solvents (Table S7†). Hence, the present computational study concludes that there is the presence of delocalized charge resonance states as an intermediate in the SB-CS and that the solvent polarity simplifies the process.

### Femtosecond transient absorption (TA) studies

To delve deeper into the solvent-modulated excited state dynamics of various structural PMI-dimers/trimer, femtosecond transient absorption (fs-TA) measurements<sup>73,74</sup> were performed in solvents of varying polarities. The 2D contour of fs-TA data for each compound in  $\text{CHCl}_3$  together with the corresponding steady-state and pump-probe laser spectra are shown in Fig. S41.† The fs-TA spectra at different probe delays for the monomer, *ortho*-PMI dimer and the self-coupled dimer are shown in Fig. 5 and for the *meta*-PMI dimer and *para*-PMI dimer, and those for the PMI-trimer are shown in Fig. S42.† The monomeric *o*-PMI-ac shows a ground state bleach (GSB) signal which corresponds to the  $S_0 \rightarrow S_1$  transition, i.e., re-absorption

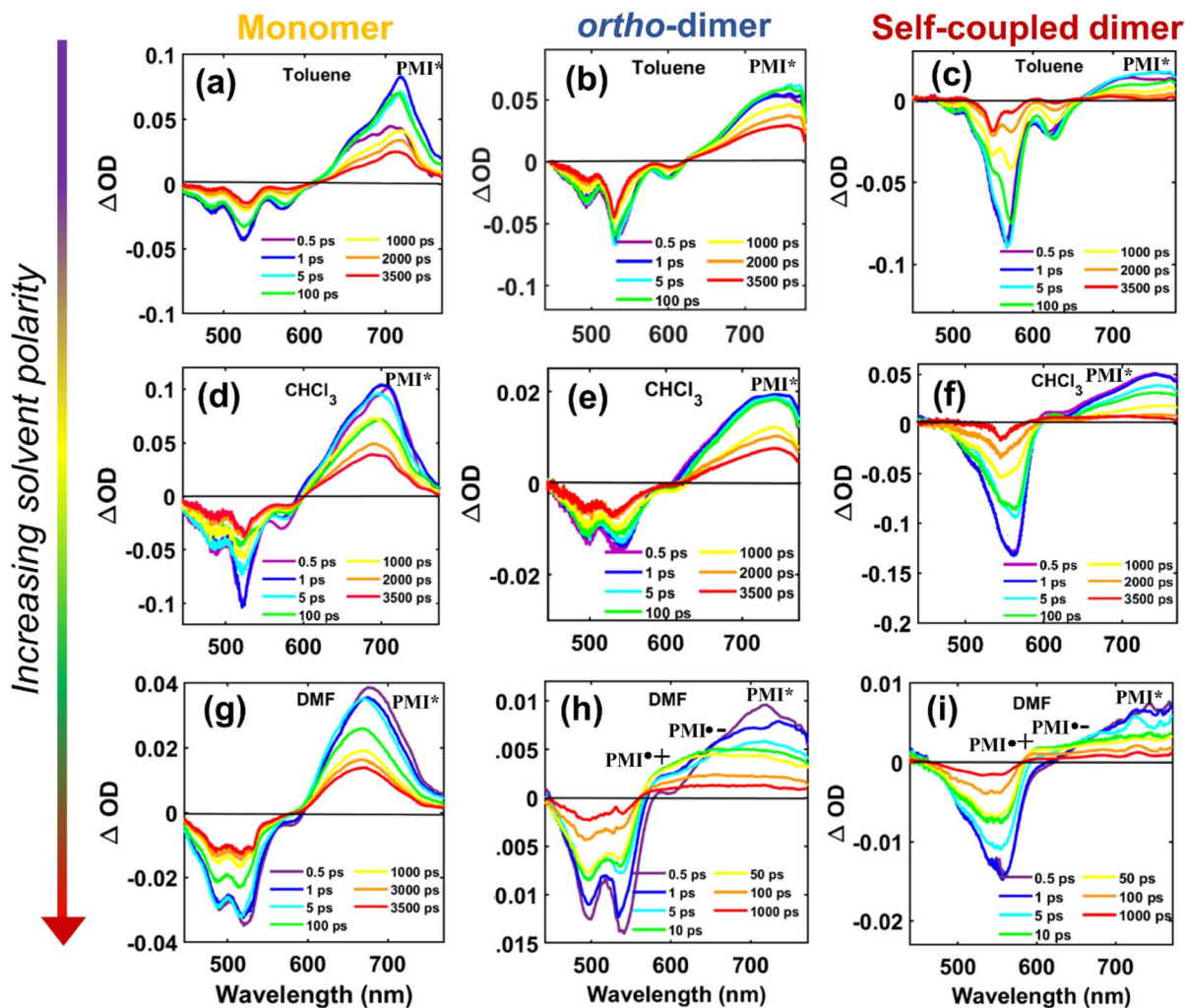


Fig. 5 Plots for transient absorption spectral traces at various probe delay times for the monomer (left panel), the *ortho*-PMI dimer (middle panel), and the self-coupled dimer (right panel) in toluene (a, b, c),  $\text{CHCl}_3$  (d, e, f), and DMF (g, h, i), respectively. The assignment of the ESA bands corresponding to the radical species is done on the basis of the spectroelectrochemistry data (Section VII in the ESI†).



from the ground state bleach (GSB) containing three different vibronic bands at 450 nm, 482 nm, and 520 nm, were quite similar to what was observed in the steady-state absorption spectrum. A stimulated emission (SE) band corresponds to the  $S_1 \rightarrow S_0$  transition is observed at around 570 nm, which was nearly comparable to the  $0 \rightarrow 1$  vibronic band in the emission spectrum; and the  $0 \rightarrow 0$  band is spectrally indistinguishable from that of the  $0 \leftarrow 0$  band of the GSB at 520 nm. The excited singlet state absorption (ESA) corresponding to the  $S_n \leftarrow S_1$  transition is observed in the 620–750 nm region. A slightly blue-shifted (compared with toluene), ESA band in  $\text{CHCl}_3$  and DMF exhibits a rise in intensity followed by decay, over longer probe delays. An observable red shift in the steady state emission spectrum of the monomer (Fig. S26†) and an increase in the single-exponential fluorescence lifetime with an increase in the solvent polarity (4.1 ns in Tol to 4.5 ns in DMF, Table S2†) is indicative of the ICT characteristic present in the monomer ***o*-PMI-ac**.

The fs-TA data of monomer ***o*-PMI-ac** in different polar solvents were reproduced well by the global lifetime fitting analysis, where the two relaxation processes are assumed to be taking place in a sequential pathway. Such global analysis of the fs-TA data enables a holistic understanding of the excited state dynamics by exploiting multiple spectrally overlapped signals and by examining these signals simultaneously, a comprehensive perspective of the behavior of the excited state can be obtained.<sup>74</sup> A two-step sequential model as shown in Fig. 6a,  $A \rightarrow B \rightarrow \text{GS}$  was employed to fit the excited-state photophysics of the monomer. The corresponding evolution-associated difference spectra (EADS) together with the population dynamics and time constants are shown in Fig. S43† and Table 3, respectively. The first relaxation process  $A \rightarrow B$  is assigned to the relaxation from the Franck–Condon (FC) region to a fully-relaxed (FR) region of the initially populated LE singlet state (state A), and eventually to an ICT state (state B) with a time constant ( $\tau_1$  or  $\tau_{A \rightarrow B} \equiv \tau_{\text{VR} + \text{FR} \rightarrow \text{ICT}}$ ) of 3.8 ps in Tol. This time constant was found to become faster on increasing the solvent polarity to 2.62

ps and 2.25 ps in  $\text{CHCl}_3$  and DMF, respectively. The second time constant ( $\tau_2$  or  $\tau_{B \rightarrow \text{GS}}$ ) ranging from 3–4 ns was attributed to the decay of the B state back to the ground state, and this time scale matches well with the fluorescence lifetime (Table S2†). To show the quality of the fitting results, the kinetics at a few selected wavelengths are shown in Fig. S44.† The choice of this kinetic model ( $A \rightarrow B \rightarrow \text{GS}$ ) is justified by the progressive red-shift in the fluorescence spectra as well as the increase in fluorescence lifetime with increasing solvent polarity, as mentioned earlier.

In a weakly polar solvent Tol and a medium polar solvent  $\text{CHCl}_3$ , the fs-TA spectra of the monomer of all the dimers and trimer resemble the steady-state absorption features in the GSB signal and a far red-shifted ESA signal occurs at around 745 nm, as shown in Fig. 5 and S42.† A red-shifted GSB, and ESA signals of different (***o*-PMI-ac**)<sub>2</sub> dimers and trimer, when compared to the monomer, is indicative of the difference in the electronic couplings between the monomeric PMI moiety present at various molecular conformational constraints within the dimer<sup>44,45</sup> as discussed in the previous section.

Contrary to the steady-state absorption spectrum, the *ortho*-dimer shows a maximum intensity at the  $0 \leftarrow 0$  band in the TA spectrum. This is primarily because this band results from the overlap of the GSB and the SE signal, as shown in Fig. 5 (middle panel). For, the *ortho*-PMI dimer in toluene and  $\text{CHCl}_3$ , the spectral features resembled the monomer, however, the kinetics varied significantly. To extract the excited-state deactivation process of the *ortho*-dimer in Tol and  $\text{CHCl}_3$ , the best-fitting results were obtained when a two-step sequential model  $A \rightarrow B \rightarrow \text{GS}$  (Fig. 6a) was employed. The EADS for the *ortho*-PMI dimer in Tol and  $\text{CHCl}_3$  are shown in Fig. 7a and b, respectively, and the corresponding population kinetics are shown in Fig. 7d–f. The first relaxation process  $A \rightarrow B$  is assigned to the relaxation from the Franck–Condon region to a fully-relaxed region of the initially populated mixed state (state A) of the Frenkel and CT excitons with a shorter lifetime component ( $\tau_1$  or  $\tau_{A \rightarrow B}$ ). This time component becomes faster in  $\text{CHCl}_3$  ( $\tau_1$  or  $\tau_{A \rightarrow B} = 0.62$  ps) when

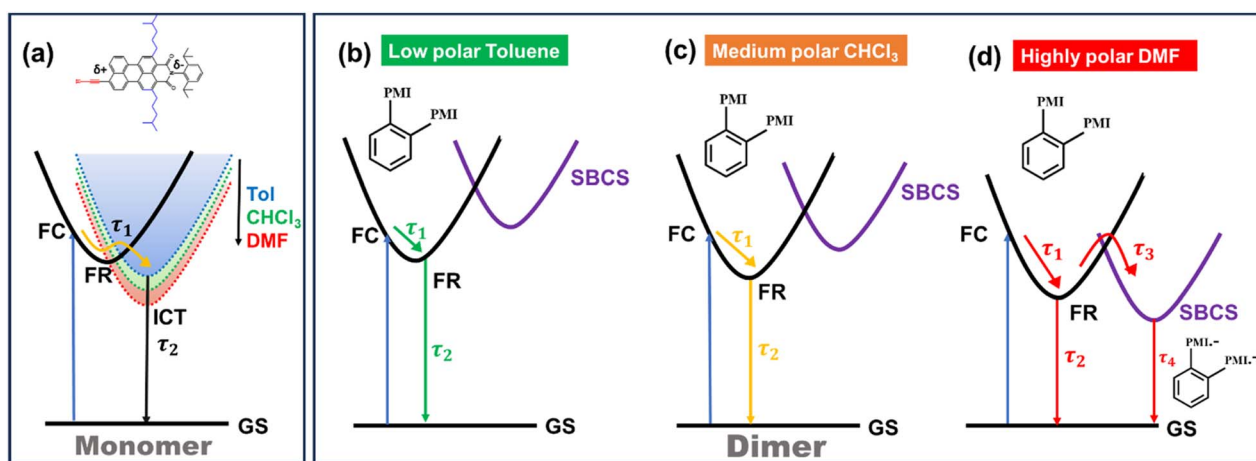
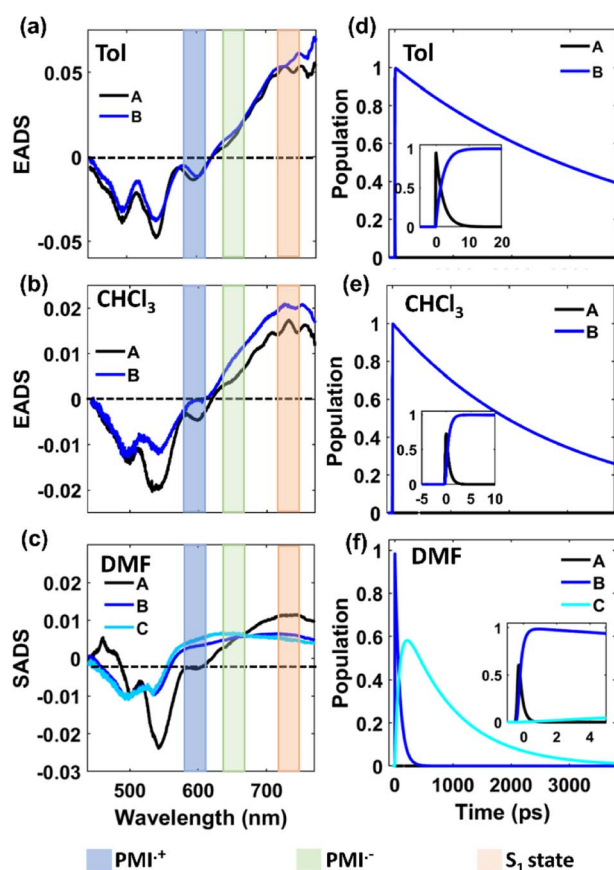


Fig. 6 Schematic potential energy diagram showing (a) solvent-dependent stabilization of charge transfer state in monomer and (b–d) different relaxation pathways for dimers after photoexcitation in lower polarity solvent toluene (b), in medium polarity solvents  $\text{CHCl}_3$  (c) and in highly polar solvent DMF (d).

Table 3 Time constants obtained from the global target analysis of the fs-TA data for toluene, CHCl<sub>3</sub>, and DMF

Compound	Solvent	$\tau_1$ or $\tau_{A \rightarrow B} \equiv \tau_{VR+FR \rightarrow ICT}$ (ps)	$\tau_2$ or $\tau_{B \rightarrow GS} \equiv \tau_{FI}$ (ps)	$\tau_3$ or $\tau_{B \rightarrow C} \equiv \tau_{SB-CS}$ (ps)	$\tau_4$ or $\tau_{C \rightarrow GS} \equiv \tau_{CR}$ (ps)
Monomer	Tol	$3.80 \pm 0.02$	$3628 \pm 1$	—	—
	CHCl <sub>3</sub>	$2.62 \pm 0.01$	$4260 \pm 6$	—	—
	DMF	$2.15 \pm 0.006$	$3670 \pm 2$	—	—
<i>ortho</i> -Dimer	Tol	$2.13 \pm 0.01$	$4053 \pm 2$	—	—
	CHCl <sub>3</sub>	$0.62 \pm 0.004$	$3824 \pm 1$	—	—
	DMF	$0.21 \pm 0.005$	$1730^a$	$80.2 \pm 0.01$	$901 \pm 2$
<i>meta</i> -Dimer	Tol	$1.13 \pm 0.004$	$3148 \pm 7$	—	—
	CHCl <sub>3</sub>	$53.7 \pm 0.1$	$3004 \pm 2$	—	—
	DMF	$4.1 \pm 0.04$	$900^a$	$2913 \pm 115$	$4545 \pm 10$
<i>para</i> -Dimer	Tol	$2.58 \pm 0.006$	$1788 \pm 0.3$	—	—
	CHCl <sub>3</sub>	$1.81 \pm 0.05$	$2129 \pm 0.9$	—	—
	DMF	$0.63 \pm 0.002$	$3600^a$	$90.8 \pm 0.38$	$851.2 \pm 3$
Self-coupled dimer	Tol	$17.6 \pm 0.02$	$1351 \pm 0.27$	—	—
	CHCl <sub>3</sub>	$1.64 \pm 0.009$	$1481 \pm 0.6$	—	—
	DMF	$0.16 \pm 0.006$	$3380^a$	$83.1 \pm 0.01$	$1012 \pm 5$
Trimer	Tol	$2.01 \pm 0.008$	$2322 \pm 0.5$	—	—
	CHCl <sub>3</sub>	$0.27 \pm 0.001$	$2332 \pm 7.1$	—	—
	DMF	$0.23 \pm 0.004$	$800^a$	$3.92 \pm 0.003$	$1268 \pm 0.6$

<sup>a</sup> Fixed lifetime values derived from TCSPC.Fig. 7 Plots of EADS and population kinetics of the *ortho*-PMI dimer ( $\lambda_{\text{ex}} = 530$  nm) in toluene (a, d), CHCl<sub>3</sub> (b, e), and DMF (c, f), respectively. Black for LE, blue for CT and cyan for SB-CS.

compared to toluene ( $\tau_1$  or  $\tau_{A \rightarrow B} = 2.13$  ps). The FR state (B state) further decays to the ground state ( $B \rightarrow \text{GS}$ ) with a lifetime component ( $\tau_2$  or  $\tau_{B \rightarrow \text{GS}}$ ) of 4.2 ns or 3.6 ns in toluene or CHCl<sub>3</sub>,

respectively, which is in agreement with the fluorescence lifetimes (see Table S2†). A progressive red shift in the stimulated emission signal in the second EADS (blue) (Fig. 7e) indicated the emergence of a novel transient species characterized by dipolar character (state B), represented as the relaxed S<sub>1</sub> state or as the charge transfer (CT) state in a previous report.<sup>46</sup> However, in the present case, this state can be labelled as the fully relaxed mixed state of the Frenkel and CT excitons (FR state). The comparison of the time constants obtained from the global analysis in Tol, CHCl<sub>3</sub>, is summarized in Table 3. Clearly, the charge separated state is not energetically accessible *via* symmetry-breaking charge separation (SB-CS) in Tol or CHCl<sub>3</sub>, which is further evident from the absence of any spectral signature of PMI<sup>++</sup> in these three solvents, and the Gibbs free energy calculations ( $\Delta G_{\text{CS}} = +0.46$  eV and  $+0.11$  eV in Tol and CHCl<sub>3</sub>, respectively). This also correlates well with the large fluorescence quantum yields in toluene ( $\Phi_{\text{F}} = 75\%$ ) and CHCl<sub>3</sub> ( $\Phi_{\text{F}} = 64\%$ ). The absence of any distinct charge-separated radical cation and anion absorption bands for PMI in Tol and CHCl<sub>3</sub> indicates that the SB-CS state lies energetically higher than the FR state in these solvents as shown in Fig. 6b and c. Interestingly, in the highly polar solvent DMF, the ESA band near 700 nm decays promptly at a longer delay time which was accompanied by a concomitant growth of a new band near 600 nm with a positive  $\Delta\text{OD}$ . The evolution of a 590 nm band associated with an isosbestic point of 650 nm nearby indicates the formation of new transient species (PMI radical cation and anion, PMI<sup>++</sup> and PMI<sup>-</sup>). The spectral evidence of the PMI<sup>++</sup> species centred on one PMI monomer in the TA spectra substantiated the generation of the PMI<sup>-</sup> also in another identical PMI unit which showed a spectral signature at 640 nm.<sup>75,76</sup> The formation of a radical cation/anion is corroborated by the chemical oxidation and spectroelectrochemistry studies (see the ESI†). However, due to the close-lying absorptions of PMI<sup>++</sup> and PMI<sup>-</sup>, we observed a single broad ESA band. The presence of such a radical species is a clear indication of solvent-mediated SB-



CS between the two PMI moieties in DMF.<sup>36,46</sup> In DMF the energy level of the SB-CS state can be effectively stabilized by solvation, bringing it below the mixed FR state, from where the charge separation is energetically favorable. Because the FR state can relax *via* both radiative (fluorescence) and non-radiative (to the SB-CS state) relaxation pathways, a branching of the population of the FR state is expected. Additionally, the existence of an equilibrium mechanism allowing both forward and backward charge transfer processes would typically lead to an enhanced fluorescence lifetime and quantum yield of the FR state.<sup>46,72,77</sup> However, it is important to note that such enhancements were not observed in the case of DMF because the SB-CS state is energetically much lower than the FR state, allowing for no back-transfer of the population. Therefore, based on the energetics, we infer that both the FR and SB-CS states are emissive and the emission from the SB-CS state results from radiative charge recombination. This justifies our choice of a kinetic model for SB-CS in DMF involving population branching leading to a dual fluorescence which, due to spectral overlap, exhibits a biexponential lifetime in the TCSPC measurements. To explain this, a global target analysis of the fs-TA data was performed. The species-associated difference spectra (SADS) obtained from the target analysis employing the kinetic scheme considered a branching of the population (Fig. 6d) using a kinetic model  $A \rightarrow B \xrightarrow{C} GS$  where state C is the SB-CS state. The corresponding SADS and population dynamics obtained from global fitting of the TA data in DMF are shown in Fig. 7c and f, respectively. Selected kinetic traces were superimposed on fitted curves at different wavelengths obtained from the global and target analysis, and these were chosen to display the fitting qualities shown in Fig. S45.† SADS 1 is ascribed to the FC state (state A), which evolves into a FR state (state B) as shown by SADS 2 in  $\tau_1$  or  $\tau_{A \rightarrow B} = 0.21$  ps. This state B further evolves into a fully charge-separated state or SB-CS state (state C) ( $PMI^{+\bullet}-PMI^{\bullet-}$ ) *via* symmetry breaking as shown by SADS 3 with a time constant ( $\tau_2$  or  $\tau_{B \rightarrow C}$ ) of 80.2 ps. This SB-CS state (state C) obtained in a highly polar solvent undergoes radiative charge recombination to the GS with a lifetime component ( $\tau_3$  or  $\tau_{C \rightarrow GS}$ ) of 901 ps (the long lifetime of 901 ps of the SB-CS state is indicative of radiative decay which also explains the biexponential nature of the fluorescence lifetime of the dimer in DMF). The fluctuations in density observed in polar solvents are always accompanied by stochastic variations in the orientation of the solvent dipoles which may effectively disrupt the symmetrical nature of the dimeric system and lead to the emergence of a larger net dipole moment, thereby decreasing the energy level of the charge separation state. This phenomenon drives the relaxation of the FR towards the SB-CS state.<sup>78</sup> The CT in the *ortho*-PMI dimer is governed predominantly by through-space coupling between the PMI chromophores and to some extent by through-bond coupling which is also evident from a negative ( $-0.004$  Å) bond-length alternation (BLA) of a covalent phenyl linker (see the Computational section of the ESI†).

For the self-coupled dimer, which forms a J-type dimer, photoexcitation at 550 nm directly excites the molecule to the hot vibrational energy levels of the singlet state,  $S_1$ . The fs-TA spectral traces at the indicated probe wavelengths of different polarities are shown in Fig. 5c, f, and 5i, and a simplified kinetic

scheme is proposed to explain the observed results (Fig. 8). A two-step sequential model,  $A \rightarrow B \rightarrow GS$  (similar to that used for the *ortho*-dimer in Tol, and  $CHCl_3$  as shown in Fig. 6b and c is used to extract the time constants of the corresponding excited-state processes that are shown in Table 3, and the corresponding EADS time-dependent concentration kinetics are shown in Fig. 8. Kinetics traces at several selected typical wavelengths are depicted in Fig. S46† and show the good quality of the fitting results. For Tol and  $CHCl_3$ , the first time constant ( $\tau_1$  or  $\tau_{A \rightarrow B}$ ) corresponds to relaxation of the FC state (state A) to the FR state (state B) and a longer time scale corresponds to the decay of the FR state to the GS ( $\tau_2$  or  $\tau_{B \rightarrow GS}$ ), which is in agreement with the fluorescence lifetime from the FR state. The formation of the FR state ( $\tau_1$  or  $\tau_{A \rightarrow B}$ ) is found to be dependent on the polarity of the solvent (Table 3) and is significantly slower in the case of the self-coupled dimer (16.1 ps/1.64 ps) when compared to the *ortho*-dimer (2.13 ps/0.62 ps) in Tol/ $CHCl_3$ , respectively. In the formation of the SB-CS state in toluene, and  $CHCl_3$  it is not evident which is also supported by the high fluorescence quantum yield of these dimers in these solvents (Tables 2 and 1) and these results are consistent with the fs-TA data.

For the self-coupled dimer in DMF, a kinetic model including the population branching (similar to *ortho*-PMI dimer in DMF, Fig. 6d) is considered. A clear appearance of a new ESA

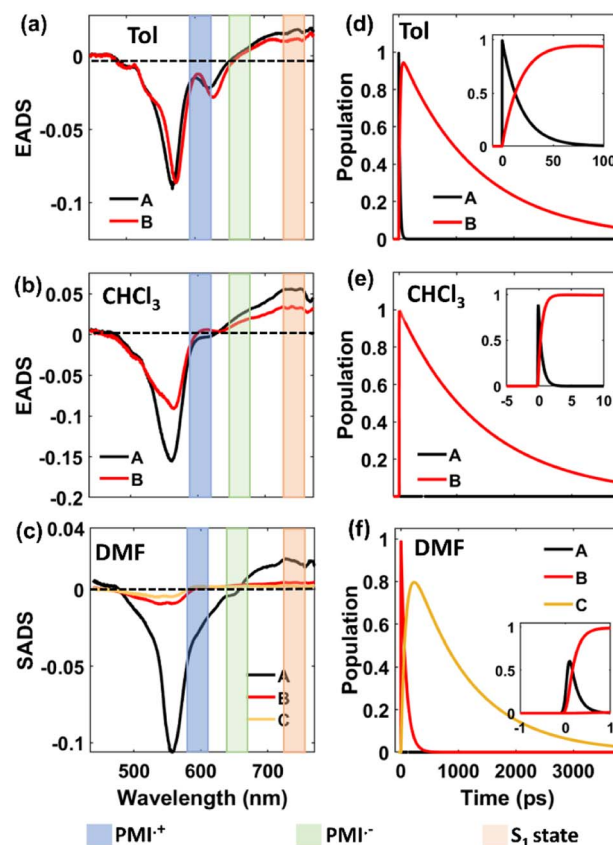


Fig. 8 Plots of EADS and population kinetics of the self-coupled dimer ( $\lambda_{ex} = 550$  nm) in toluene (a, d),  $CHCl_3$  (b, e), and DMF (c, f), respectively.





band at 590 nm corresponded to the formation of  $\text{PMI}^{+}$  and the spectral signature of  $\text{PMI}^{-}$  showed a positive absorption at 640 nm which overlapped with the ESA of the FC state (state A), and indicated SB-CS, as shown in Fig. 5i. The results for the obtained SADS are shown in Fig. 8c together with the population kinetics (Fig. 8f). The SB-CS formation rate in DMF, is found to be comparable for both the *ortho*-dimer  $k_{\text{SB-CS}} = 0.0124 \text{ ps}^{-1}$  and for the self-coupled dimer  $k_{\text{SB-CS}} = 0.012 \text{ ps}^{-1}$ .

In the case of the *meta*-, *para*-PMI dimers and trimer, the excited state relaxation process varies differently with the change in the solvent polarity as shown in Fig. S42.† Fig. S47–S49† (ESI) shows the results of the global target analysis employing a similar kinetic model (Fig. 6) as used for the *ortho*-dimer and the self-coupled dimer, and for the *meta*-dimer, *para*-dimer and trimer in various solvents, and the corresponding relaxation time constants are summarized in Table 3. Kinetic traces at selected wavelengths are shown in Fig. S50–S52† and show the quality of fit. In toluene and  $\text{CHCl}_3$ , the results can be rationalized in a similar way as for the *ortho*- and self-coupled dimers. The two major processes participating in excited state relaxation in Tol,  $\text{CHCl}_3$  are relaxation of the FC (state A) to the FR (state B) followed by the decay of the FR state to the GS. A comparison of solvent-dependent relaxation kinetics of these dimers shows a slower relaxation of the equilibrated state to the GS for the *meta*-PMI dimer when compared to *para*-PMI dimer and trimer in Tol and  $\text{CHCl}_3$ , which is also in agreement with the observed fluorescence lifetimes (Table S2†). In a higher polarity solvent, DMF, it was clear that for the trimer, the initial SADS 1 is dominated by a strong artifact which is ascribed to the FC state (state A) as shown in Fig. S49c (ESI).† This state further evolves to a FR state (state B) as shown by SADS 2 and finally into a SB-CS state (state C) as shown by SADS 3 with a time constant ( $\tau_2$  or  $\tau_{\text{B} \rightarrow \text{C}}$ ) of 3.92 ps. This is further evident from the diminished negative SE band and a positive ESA band in the region from 590 nm to 630 nm. However, the SADS obtained for the *meta*-dimer and *para*-dimer (Fig. S47c and 48c†) did not show any such switching of  $\Delta\text{OD}$  (SE to ESA). These findings suggest the presence of a different predominant non-radiative relaxation mechanism in these two dimers (which may be attributed to solvent fluctuations, and conformational relaxation<sup>77</sup>), effectively decreasing the degree of coupling between the FC and CT states necessary for SB-CS<sup>78</sup> and also leading to a decrease in the fluorescence lifetime.

However, it should be noted that the absence of a characteristic spectrum for  $\text{PMI}^{-}$  or  $\text{PMI}^{+}$  in SADS for the *meta*- and *para*-dimers may arise due to the masking of this band because of the overlapping spectral features. To verify this, we analyzed the kinetic traces at 590 nm (where the characteristic spectral feature of  $\text{PMI}^{+}$  for the *ortho*-dimer, self-coupled dimer and trimer appears) (Fig. S53†); the corresponding fitting parameters are summarized in Table S8†. A somewhat similar analysis was employed recently in a different context, where the kinetics of the ESA bands' intensity ratios were compared to verify the formation of a TIPS-pentacene cation in the TIPS-pentacene/MAPbI<sub>3</sub> perovskite bilayer film.<sup>79</sup> A comparison between the kinetics in toluene and DMF shows that a negative (GSB/SE) to a positive (ESA)  $\Delta\text{OD}$  upon changing the solvent from Tol to

DMF is present only for *ortho*-, self-coupled dimers and trimer but not for the *meta* or *para* dimers, which is suggestive of a less efficient SB-CS in these two dimers. This observation is also consistent with the theoretical prediction of a relatively less (when compared with the *ortho* dimer) extent of coupling between the Frenkel and CT states in these two dimers. However, the observation of fluorescence quenching and biexponential fluorescence kinetics in DMF for the *meta* and *para* dimers and the fast rate of relaxation of the FR state (90 ps) for *para*-dimer (comparable with that for the *ortho*- and self-coupled dimers, which is about 80 ps), hints that the presence of SB-CS in these two dimers cannot be completely ruled out.

### Thermodynamic feasibility of charge separation

The fs-TAS studies unravel a symmetry-breaking charge separation for the *ortho*- and self-coupled dimer in DMF which is less prominent for the trimer derivative. The formation of radical pairs *via* SB-CS is established by chemical oxidation using  $\text{SbCl}_5$  and spectroelectrochemical reduction, as given in Fig. S54 and S55.† The thermodynamic feasibility of such charge separation process can be explicated from the Gibbs free energy change ( $\Delta G_{\text{CS}}$ ) during the charge separation which can be determined from the well-known Rehm–Weller equation (eqn (8)):

$$\Delta G_{\text{CS}} = e(E_{\text{OX}} - E_{\text{RED}}) - E_{0,0} - \frac{e^2}{4\pi\epsilon_0\epsilon_s d_{\text{DA}}} - \frac{e^2}{8\pi\epsilon_0} \left( \frac{1}{r_{\text{D}}} + \frac{1}{r_{\text{A}}} \right) \times \left( \frac{1}{\epsilon_{\text{Ref}}} - \frac{1}{\epsilon_s} \right) \quad (8)$$

where,  $E_{\text{OX}}$  and  $E_{\text{RED}}$  denote the first oxidation and reduction potential of the donor PMI and acceptor PMI units, respectively, in dimers/trimer;  $E_{0,0}$  is the energy of the first excited state of the compound which can be estimated from the intercrossing point of the normalized absorption and emission spectra. The parameters  $d_{\text{DA}}$ ,  $r_{\text{A}}$ , and  $r_{\text{D}}$  are calculated from the ground state geometry of the dimer derivatives optimized by DFT at the B3LYP/6-31+g(d,p) level of theory. The  $r_{\text{D}}$  and  $r_{\text{A}}$  illustrate the effective radius of the donor radical cation and acceptor radical anion, respectively. The  $\epsilon_{\text{Ref}}$  and  $\epsilon_s$  are the dielectric constant of the reference solvent used in the electrochemical measurement and the particular solvent used for the determination of the CS. Here, the electrochemical measurements were performed in anhydrous dichloromethane (DCM).

We have estimated the  $\Delta G_{\text{CS}}$  for two dimers showing SB-CS in DMF by considering the  $E_{\text{OX}}$  and  $E_{\text{RED}}$  values from the cyclic voltammetry plots (Fig. S56†) and the previously mentioned parameters in eqn (8). The data in Table 4 shows that  $\Delta G_{\text{CS}}$  is negative ( $\Delta G_{\text{CS}} < 0$ ) in polar DMF but it is expressed as  $\Delta G_{\text{CS}} > 0$  in weakly-polar and medium-polar solvents. These values show that the charge separation is thermodynamically favorable in a polar solvent but is not feasible in weakly-polar solvents. For other dimers, a negative  $\Delta G_{\text{CS}}$  in DMF is also obtained (−0.14 eV and −0.09 eV for *meta*- and *para*-PMI dimers respectively) as shown in Table S9†, indicating the possibility of a partial charge transfer in DMF. Furthermore, the self-energy



Table 4 The Gibbs free energies determined for the charge separation of two dimers in three different solvents

Compound	Solvent	$E_{ox}/V$	$E_{red}/V$	$E_{0,0}/eV$	$r_D$ or $r_A/\text{\AA}$	$d_{DA}/\text{\AA}$	$\Delta G_{CS}$ (eV)
<i>ortho</i> -Dimer	Tol	1.43	−0.92	2.28	4.75	11.1	+0.46
	CHCl <sub>3</sub>	1.43	−0.92	2.26	4.75	11.1	+0.11
	DMF	1.43	−0.92	2.25	4.75	11.1	−0.19
Self-coupled dimer	Tol	1.36	−1.02	2.18	4.75	14.1	+0.70
	CHCl <sub>3</sub>	1.36	−1.02	2.18	4.75	14.1	+0.28
	DMF	1.36	−1.02	2.17	4.75	14.1	−0.08

correction ( $\Delta_{CT}$ ) for the *meta*-dimer cannot be neglected. The  $\Delta_{CT} = -145 \text{ cm}^{-1}$  indicates that there is an existing coupling between the local and charge-separated excitons (Table 2). Therefore, it is feasible that a partial charge transfer will be manifested in the *meta*-dimer. In certain circumstances, however, a decrease in CT-mediated coupling is made possible by an increase in spatial separation and is largely reliant on the monomer's LUMO and HOMO nodal patterns. Additionally, the CT integrals show no change in the monomer's orientation, which is a crucial solvent-related feature (Fig. S37†). A schematic illustration of SB-CS occurring here is shown in Fig. S57.†

## Further discussion

In summary, the excited state relaxation mechanism for the *ortho*-dimer and the self-coupled dimer, when considered alongside the previously mentioned outcomes, can be described as illustrated in Fig. 6. In a weakly polar solvent like Tol and the medium polar solvent CHCl<sub>3</sub>, the relaxation occurs *via* an initial relaxation of the FC state to the FR state followed by decay to the GS. In contrast, in the highly polar DMF, the solvent fluctuation leads to stabilization of the SB-CS state with a clear observation of a radical cation and the anion peaks, which were not so prominent for the *meta*-, *para*-dimer and trimer. The distinctly different excited-state dynamics of all the dimers are mainly attributed to the different molecular geometries. In both the *ortho*- and self-coupled dimer, the rate of charge recombination is obtained much slower than the rate of charge separation [for the *ortho*-dimer,  $k_{CR} = (901 \text{ ps})^{-1}$  whereas  $k_{SB-CS} = (80.2 \text{ ps})^{-1}$ ] in DMF which is quite an exothermic process due to the prevailing Marcus inverted region,<sup>16</sup> and is also evident from the negative  $\Delta G_{CS}$  in DMF (Tables 3 and 4). The branching ratio for the FR state population decayed into the radiative channel and the SB-CS state can be attained by considering the relative rates:

$\frac{k_3}{k_2 + k_3} = \frac{1/\tau_3}{1/\tau_2 + 1/\tau_3}$ . This estimate shows that ~95% of the population branches into the SB-CS channel in the *ortho*-dimer whereas it is ~80% for the self-coupled dimer. It should be noted that the SB-CS state may undergo a further additional deactivation pathway, which involves the recombination of the charge-separated state to populate the triplet state, thus lowering the possibility of the crucially important long-lived charge separation, essential for the photovoltaic application.<sup>3,80</sup> However, in the present study, the lack of any long-lived component and any distinctive features for the <sup>3</sup>PMI state in the TA spectra of dimers and trimer suggests the absence of any

triplet state formation.<sup>44,47</sup> A summary of charge separation and charge recombination time constants ( $\tau$ ) of PDI and PMI-based multichromophoric systems has been provided in Table S10†.

## Conclusions

To summarize, we have presented here a design strategy to construct a series of covalently linked alkyne-bridged PMI-based multichromophores and thoroughly investigated the impact of positional isomerism on the SB-CS phenomenon. Steady-state spectroscopic measurements showed a considerable red shift in the emission spectra when the solvent polarity was increased. In highly polar DMF, a huge decrease in fluorescence QY and alteration of fluorescence lifetime indicates the possibility of charge separation and further stabilization of the charge-separated state. Ultrafast charge separation and charge recombination in DMF for the *ortho*- and self-coupled dimers in this series were established using a femtosecond transient absorption study. For other dimers, the relaxation of the excited state occurs *via* structural relaxation and the trimer was found to show some reminiscent of SB-CS. The underlying difference in the relaxation mechanism was evident from the femtosecond transient studies, which arose principally from the difference in the interchromophore coupling among the PMI units in different regioisomers. The twisted conformation is responsible for making a weakly coupled system which becomes favorable for SB-CS. Additionally, the theoretical studies provide strong evidence for predominant charge transfer characteristics between two identical chromophores in the *ortho*-PMI dimer rather than the *meta*- and *para*-congeners which is attributed mostly to the through-space coupling and some extent to the through-bond coupling between two PMI units. The two isomers exhibiting high thermal and chemical stability, large synthetic scalability and more importantly, notable charge separation characteristics can be exploited as potential candidates for their application in modern organic photovoltaics.

## Data availability

The data can be available upon request from the corresponding author.

## Author contributions

RR synthesized all the compounds, purified them, and characterized them by HRMS and NMR spectroscopic techniques. RR



also performed steady-state UV-Vis absorption, fluorescence, and TCSPC for lifetime and electrochemical measurements. SC and YS performed all the femtosecond transient absorption measurements and their analysis was supervised by AKD. VS designed the synthesis of the molecules used in this project and optimized the synthetic protocols. The theoretical calculations were performed by AKP. The initial draft of the manuscript was made by RR, SC, AKP, and YS. The final draft of the manuscript was revised by AD, AKD and ALK after receiving data from the other authors. Analysis and interpretation of data were done by all the authors. All the authors have approved the final version of the manuscript.

## Conflicts of interest

There are no conflicts to declare.

## Acknowledgements

RR and VS acknowledge IISER Bhopal and CSIR, respectively, for their doctoral fellowships. SC and YS both acknowledge IISER Mohali for their doctoral fellowships. AKP sincerely acknowledges Technical Research Center (TRC) in IACS Kolkata for the Research Associate fellowship. RR and ALK convey thanks to the Central Instrumental Facility in IISER Bhopal. ALK thanks IISER Bhopal for the research funding. AKD acknowledges SERB, DST (CRG/2021/003981) and IISER Mohali for funding. AD thanks SERB (CRG/2020/000301) for financial support.

## Notes and references

- 1 E. Vauthey, *ChemPhysChem*, 2012, **13**, 2001–2011.
- 2 A. N. Bartynski, M. Gruber, S. Das, S. Rangan, S. Mollinger, C. Trinh, S. E. Bradforth, K. Vandewal, A. Salles, R. A. Bartynski, W. Bruetting and M. E. Thompson, *J. Am. Chem. Soc.*, 2015, **137**, 5397–5405.
- 3 E. Sebastian and M. Hariharan, *ACS Energy Lett.*, 2022, **7**, 696–711.
- 4 M. Kellogg, A. Akil, D. S. Muthiah Ravinson, L. Estergreen, S. E. Bradforth and M. E. Thompson, *Faraday Discuss.*, 2019, **216**, 379–394.
- 5 A. I. Ivanov, B. Dereka and E. Vauthey, *J. Chem. Phys.*, 2017, **146**, 164306.
- 6 A. Aster, G. Licari, F. Zinna, E. Brun, T. Kumpulainen, E. Tajkhorshid, J. Lacour and E. Vauthey, *Chem. Sci.*, 2019, **10**, 10629–10639.
- 7 M. Söderberg, B. Dereka, A. Marrocchi, B. Carlotti and E. Vauthey, *J. Phys. Chem. Lett.*, 2019, **10**, 2944–2948.
- 8 W. Kim, T. Kim, S. Kang, Y. Hong, F. Würthner and D. Kim, *Angew. Chem., Int. Ed.*, 2020, **59**, 8571–8578.
- 9 B. Dereka, D. Svechkarev, A. Rosspeintner, A. Aster, M. Lunzer, R. Liska, A. M. Mohs and E. Vauthey, *Nat. Commun.*, 2020, **11**, 1925.
- 10 C. Lee, C. H. Choi and T. Joo, *Phys. Chem. Chem. Phys.*, 2020, **22**, 1115–1121.
- 11 P. D. Laible, D. K. Hanson, J. C. Buhrmaster, G. A. Tira, K. M. Faries, D. Holten and C. Kirmaier, *Proc. Natl. Acad. Sci. U.S.A.*, 2020, **117**, 865–871.
- 12 J. H. Golden, L. Estergreen, T. Porter, A. C. Tadler, D. Sylvinson, M. R. J. W. Facendola, C. P. Kubiak, S. E. Bradforth and M. E. Thompson, *ACS Appl. Energy Mater.*, 2018, **1**, 1083–1095.
- 13 R. M. Young and M. R. Wasielewski, *Acc. Chem. Res.*, 2020, **53**, 1957–1968.
- 14 Y. Hong, F. Schlosser, W. Kim, F. Würthner and D. Kim, *J. Am. Chem. Soc.*, 2022, **144**, 15539–15548.
- 15 K. Wang, G. Shao, S. Peng, X. You, X. Chen, J. Xu, H. Huang, H. Wang, D. Wu and J. Xia, *J. Phys. Chem. B*, 2022, **126**, 3758–3767.
- 16 C. Lin, T. Kim, J. D. Schultz, R. M. Young and M. R. Wasielewski, *Nat. Chem.*, 2022, **14**, 786–793.
- 17 F. C. Grozema, M. Swart, R. W. J. Zijlstra, J. J. Piet, L. D. A. Siebbeles and P. T. van Duijnen, *J. Am. Chem. Soc.*, 2005, **127**, 11019–11028.
- 18 T. Takaya, S. Saha, H.-o. Hamaguchi, M. Sarkar, A. Samanta and K. Iwata, *J. Phys. Chem. A*, 2006, **110**, 4291–4295.
- 19 Y. Liu, J. Zhao, A. Iagatti, L. Bussotti, P. Foggi, E. Castellucci, M. Di Donato and K.-L. Han, *J. Phys. Chem. C*, 2018, **122**, 2502–2511.
- 20 M. T. Whited, N. M. Patel, S. T. Roberts, K. Allen, P. I. Djurovich, S. E. Bradforth and M. E. Thompson, *Chem. Commun.*, 2012, **48**, 284–286.
- 21 V. Markovic, D. Villamaina, I. Barabanov, L. M. Lawson Daku and E. Vauthey, *Angew. Chem., Int. Ed.*, 2011, **50**, 7596–7598.
- 22 R. E. Cook, B. T. Phelan, R. J. Kamire, M. B. Majewski, R. M. Young and M. R. Wasielewski, *J. Phys. Chem. A*, 2017, **121**, 1607–1615.
- 23 G. Ran, J. Zeb, Y. Song, P. A. Denis, U. Ghani and W. Zhang, *J. Phys. Chem. C*, 2022, **126**, 3872–3880.
- 24 N. E. Powers-Riggs, X. Zuo, R. M. Young and M. R. Wasielewski, *J. Am. Chem. Soc.*, 2019, **141**, 17512–17516.
- 25 C. Trinh, K. Kirlikovali, S. Das, M. E. Ener, H. B. Gray, P. Djurovich, S. E. Bradforth and M. E. Thompson, *J. Phys. Chem. C*, 2014, **118**, 21834–21845.
- 26 Z. Mahmood, N. Rehmat, S. Ji, J. Zhao, S. Sun, M. Di Donato, M. Li, M. Teddei and Y. Huo, *Chem. - Eur. J.*, 2020, **26**, 14912–14918.
- 27 T. Kim, J. Kim, H. Mori, S. Park, M. Lim, A. Osuka and D. Kim, *Phys. Chem. Chem. Phys.*, 2017, **19**, 13970–13977.
- 28 M. Cacioppo, T. Scharl, L. Đorđević, A. Cadranel, F. Arcudi, D. M. Guldi and M. Prato, *Angew. Chem., Int. Ed.*, 2020, **59**, 12779–12784.
- 29 P. Roy, G. Bressan, J. Gretton, A. N. Cammidge and S. R. Meech, *Angew. Chem., Int. Ed.*, 2021, **60**, 10568–10572.
- 30 B. Dereka, A. Rosspeintner, Z. Li, R. Liska and E. Vauthey, *J. Am. Chem. Soc.*, 2016, **138**, 4643–4649.
- 31 I. Papadopoulos, M. J. Álvaro-Martins, D. Molina, P. M. McCosker, P. A. Keller, T. Clark, Á. Sastre-Santos and D. M. Guldi, *Adv. Energy Mater.*, 2020, **10**, 2001496.
- 32 J. S. Beckwith, A. Rosspeintner, G. Licari, M. Lunzer, B. Holzer, J. Fröhlich and E. Vauthey, *J. Phys. Chem. Lett.*, 2017, **8**, 5878–5883.





- 33 B. Dereka, A. Rosspeintner, R. Stężycki, C. Ruckebusch, D. T. Gryko and E. Vauthey, *J. Phys. Chem. Lett.*, 2017, **8**, 6029–6034.
- 34 X. Niu, Z. Kuang, M. Planells, Y. Guo, N. Robertson and A. Xia, *Phys. Chem. Chem. Phys.*, 2020, **22**, 15743–15750.
- 35 P. Su, H. Liu, L. Shen, J. Zhou, W. Wang, S. Liu, X. Nie, Z. Li, Z. Liu, Y. Chen and X. Li, *Mater. Chem. Front.*, 2022, **6**, 707–717.
- 36 E. Sebastian and M. Hariharan, *J. Am. Chem. Soc.*, 2021, **143**, 13769–13781.
- 37 V. Sharma, J. D. B. Koenig and G. C. Welch, *J. Mater. Chem. A*, 2021, **9**, 6775–6789.
- 38 F. Würthner, C. R. Saha-Möller, B. Fimmel, S. Ogi, P. Leowanawat and D. Schmidt, *Chem. Rev.*, 2016, **116**, 962–1052.
- 39 R. Roy, N. R. Sajeev, V. Sharma and A. L. Koner, *ACS Appl. Mater. Interfaces*, 2019, **11**, 47207–47217.
- 40 O. Chatterjee, R. Roy, A. Pramanik, T. Dutta, V. Sharma, P. Sarkar and A. L. Koner, *Adv. Opt. Mater.*, 2022, **10**, 2201187.
- 41 C. Li and H. Wonneberger, *Adv. Mater.*, 2012, **24**, 613–636.
- 42 N. Zink-Lorre, S. Seetharaman, D. Gutiérrez-Moreno, F. Fernández-Lázaro, P. A. Karr and F. D'Souza, *Chem. - Eur. J.*, 2021, **27**, 14996–15005.
- 43 V. Piradi, Y. Gao, F. Yan, M. Imran, J. Zhao, X. Zhu and S. K. So, *ACS Appl. Energy Mater.*, 2022, **5**, 7287–7296.
- 44 Y. Wu, R. M. Young, M. Frascioni, S. T. Schneckel, P. Spenst, D. M. Gardner, K. E. Brown, F. Würthner, J. F. Stoddart and M. R. Wasielewski, *J. Am. Chem. Soc.*, 2015, **137**, 13236–13239.
- 45 J. Sung, A. Nowak-Król, F. Schlosser, B. Fimmel, W. Kim, D. Kim and F. Würthner, *J. Am. Chem. Soc.*, 2016, **138**, 9029–9032.
- 46 J. Kong, W. Zhang, G. Li, D. Huo, Y. Guo, X. Niu, Y. Wan, B. Tang and A. Xia, *J. Phys. Chem. Lett.*, 2020, **11**, 10329–10339.
- 47 Y. Guo, Z. Ma, X. Niu, W. Zhang, M. Tao, Q. Guo, Z. Wang and A. Xia, *J. Am. Chem. Soc.*, 2019, **141**, 12789–12796.
- 48 E. Sebastian, J. Sunny and M. Hariharan, *Chem. Sci.*, 2022, **13**, 10824–10835.
- 49 E. Sebastian and M. Hariharan, *Angew. Chem., Int. Ed.*, 2023, **62**, e202216482.
- 50 H. Khandelwal, A. R. Mallia, R. T. Cheriya and M. Hariharan, *Phys. Chem. Chem. Phys.*, 2012, **14**, 15282–15285.
- 51 H. Song, H. Zhao, Y. Guo, A. M. Philip, Q. Guo, M. Hariharan and A. Xia, *J. Phys. Chem. C*, 2020, **124**, 237–245.
- 52 N. Kapuria, V. Sharma, P. Kumar and A. L. Koner, *J. Mater. Chem. C*, 2018, **6**, 11328–11335.
- 53 A. Dannenhoffer, H. Sai, D. Huang, B. Nagasing, B. Harutyunyan, D. J. Fairfield, T. Aytun, S. M. Chin, M. J. Bedzyk, M. Olvera de la Cruz and S. I. Stupp, *Chem. Sci.*, 2019, **10**, 5779–5786.
- 54 R. Roy, A. Khan, O. Chatterjee, S. Bhunia and A. L. Koner, *Org. Mater.*, 2021, **3**, 417–454.
- 55 R. Roy, A. Khan, T. Dutta and A. L. Koner, *J. Mater. Chem. B*, 2022, **10**, 5352–5363.
- 56 J. Warnan, J. Willkomm, Y. Farré, Y. Pellegrin, M. Boujtita, F. Odobel and E. Reisner, *Chem. Sci.*, 2019, **10**, 2758–2766.
- 57 N. J. Hestand and F. C. Spano, *Chem. Rev.*, 2018, **118**, 7069–7163.
- 58 L. Estergreen, A. R. Mencke, D. E. Cotton, N. V. Korovina, J. Michl, S. T. Roberts, M. E. Thompson and S. E. Bradforth, *Acc. Chem. Res.*, 2022, **55**, 1561–1572.
- 59 V. Sharma, D. Sahoo, F. Chandra and A. L. Koner, *ChemistrySelect*, 2017, **2**, 11747–11754.
- 60 P. J. Brown, M. L. Williams, S. Nakamura, J. R. Palmer, R. M. Young and M. R. Wasielewski, *J. Phys. Chem. C*, 2024, **128**, 58–66.
- 61 R. Komskis, P. Adomėnas, O. Adomėnienė, P. Baronas, T. Serevičius and S. Jursėnas, *J. Phys. Chem. C*, 2019, **123**, 27344–27354.
- 62 W. Zhang, J. Kong, D. Hu, M. Tao, X. Niu, S. Vdović, D. Aumiller, Y. Ma and A. Xia, *J. Phys. Chem. C*, 2020, **124**, 5574–5582.
- 63 M. E. Madjet, A. Abdurahman and T. Renger, *J. Phys. Chem. B*, 2006, **110**, 17268–17281.
- 64 M. Kasha, *Discuss. Faraday Soc.*, 1950, **9**, 14–19.
- 65 N. J. Hestand, H. Yamagata, B. Xu, D. Sun, Y. Zhong, A. R. Harutyunyan, G. Chen, H.-L. Dai, Y. Rao and F. C. Spano, *J. Phys. Chem. C*, 2015, **119**, 22137–22147.
- 66 C. Zhong, D. Bialas and F. C. Spano, *J. Phys. Chem. C*, 2020, **124**, 2146–2159.
- 67 B. Engels and V. Engel, *Phys. Chem. Chem. Phys.*, 2017, **19**, 12604–12619.
- 68 N. J. Hestand and F. C. Spano, *Acc. Chem. Res.*, 2017, **50**, 341–350.
- 69 A. Benny, R. Ramakrishnan and M. Hariharan, *Chem. Sci.*, 2021, **12**, 5064–5072.
- 70 D. Bansal, A. Kundu, V. P. Singh, A. K. Pal, A. Datta, J. Dasgupta and P. Mukhopadhyay, *Chem. Sci.*, 2022, **13**, 11506–11512.
- 71 C. Qin, Z. Zhang, Q. Xu, J. Song, Z. Jiao, S. Ma, R. Qin and Y. Jiang, *J. Phys. Chem. Lett.*, 2023, **14**, 2455–2462.
- 72 A. F. Coleman, M. Chen, J. Zhou, J. Y. Shin, Y. Wu, R. M. Young and M. R. Wasielewski, *J. Phys. Chem. C*, 2020, **124**, 10408–10419.
- 73 Y. Silori, S. Chawla and A. K. De, *ChemPhysChem*, 2020, **21**, 1908–1917.
- 74 K. Rani, S. Chawla, V. Kumari, A. K. De and S. Sengupta, *J. Mater. Chem. C*, 2022, **10**, 10551–10561.
- 75 K. M. Lefler, D. T. Co and M. R. Wasielewski, *J. Phys. Chem. Lett.*, 2012, **3**, 3798–3805.
- 76 R. T. Cheriya, A. R. Mallia and M. Hariharan, *Energy Environ. Sci.*, 2014, **7**, 1661–1669.
- 77 J. M. Alzola, N. A. Tcyrlunikov, P. J. Brown, T. J. Marks, M. R. Wasielewski and R. M. Young, *J. Phys. Chem. A*, 2021, **125**, 7633–7643.
- 78 J. J. Piet, W. Schuddeboom, B. R. Wegewijs, F. C. Grozema and J. M. Warman, *J. Am. Chem. Soc.*, 2001, **123**, 5337–5347.
- 79 S. Lee, D. Hwang, S. I. Jung and D. Kim, *J. Phys. Chem. Lett.*, 2017, **8**, 884–888.
- 80 A. J. Gillett, A. Privitera, R. Dilmurat, A. Karki, D. Qian, A. Pershin, G. Londi, W. K. Myers, J. Lee, J. Yuan, S.-J. Ko, M. K. Riede, F. Gao, G. C. Bazan, A. Rao, T.-Q. Nguyen, D. Beljonne and R. H. Friend, *Nature*, 2021, **597**, 666–671.

